JOURNAL OF GEOPHYSICAL RESEARCH, VOL. 101, NO. B8, PAGES 17,707–17,725, AUGUST 10, 1996

The 1992 M=7 Cape Mendocino, California, earthquake: Coseismic deformation at the south end of the Cascadia megathrust

Mark H. Murray,[1,2] Grant A. Marshall,[3] Michael Lisowski,[4] and Ross S. Stein

U.S. Geological Survey, Menlo Park, California

Abstract. We invert geodetic measurements of coseismic surface displacements to determine a dislocation model for the April 25, 1992, M=7 Cape Mendocino, California, earthquake. The orientation of the model slip vector, which nearly parallels North America–Juan de Fuca relative plate convergence, and the location and orientation of the model fault relative to the offshore Cascadia megathrust, suggest that the 1992 Cape Mendocino earthquake is the first well-recorded event to relieve strain associated with the Cascadia subduction zone. We use data from three geodetic techniques: (1) the horizontal and vertical displacements of 13 monuments surveyed with the Global Positioning System, corrected for observed horizontal interseismic strain accumulation, (2) 88 section-elevation differences between leveling monuments, and (3) the uplift of 12 coastal sites observed from the die-off of intertidal marine organisms. Maximum observed displacements are 0.4 m of horizontal movement and 1.5 m of uplift along the coast. We use Monte Carlo techniques to estimate an optimal uniform slip rectangular fault geometry and its uncertainties. The optimal model using all the data resolves 4.9 m of slip on a 14 by 15 km fault that dips 28° SE. The fault extends from 1.5 to 8.7 km in depth and the main-shock hypocenter is close to the downdip projection of the fault. The shallowly dipping fault plane is consistent with the observed aftershock locations, and the estimated geodetic moment is 3.1×10^{19} N m, 70% of the seismic moment. Other models that exclude leveling data collected in 1935 and 1942 are more consistent with seismological estimates of the fault geometry. If the earthquake is characteristic for this segment, the estimated horizontal slip vector compared with plate convergence rates suggests a recurrence interval of 140 years, with a 95% confidence range of 100–670 years. The coseismic uplift occurred in a region that also has high Quaternary uplift rates determined from marine terrace studies. If repeated ruptures of this southernmost segment of the Cascadia megathrust are responsible for the Quaternary uplift, a comparison of the coseismic uplift with coastal uplift rates suggests a recurrence interval of 200–400 years. Thus comparing horizontal and vertical coseismic to long-term deformation suggests a recurrence interval of about 100–300 years for M=7 events at the south end of the Cascadia megathrust.

Introduction

The April 25, 1992, Cape Mendocino, California, earthquake (moment magnitude M=7) is the first well-recorded event to demonstrate the seismogenic potential of the Cascadia subduction zone [*Oppenheimer et al.*, 1993]. The mainshock, located 25 km southeast of Cape Mendocino at 10 km depth, and two deeper M~6.6 aftershocks located 25 km offshore, caused moderate structural damage in nearby communities. Strong ground motions and a small tsunami occurred, but surface faults did not rupture onshore. The mainshock occurred near the Mendocino triple junction, where the Pacific, North America, and Juan de Fuca plates meet. The focal mechanism and nearby aftershock locations indicate that the earthquake ruptured a shallow thrust fault dipping northeast, consistent with rupture on the southernmost segment of the Cascadia megathrust (Figure 1) [*Oppenheimer et al.*, 1993].

The Mendocino triple junction, at the intersection of the San Andreas fault system, the Mendocino transform fault, and the Cascadia megathrust, is one of the most seismically active regions in California. Over 25% of the seismic energy released by California and vicinity earthquakes during the 50-year period before 1992 occurred along or within the Gorda deformation zone [*Gee et al.*, 1991], the southernmost portion of the Juan de Fuca plate that is both subducting beneath North America in northern California and internally deforming [*Wilson*, 1986, 1989]. Most of the historic earthquakes in the area are located either in the Gorda deformation zone or along the Mendocino transform fault, and no thrust events prior to the 1992 Cape Mendocino earthquake have been recorded along the entire Cascadia subduction zone [*Dengler et al.*, 1992]. Two major earthquakes have been located near Cape Mendocino that may be associated with the megathrust. The January 22, 1923, M_s=7.3 earthquake produced an isoseismal intensity map nearly identical to that of the 1992 mainshock [*Toppozada and Parke*, 1982] but is poorly located from teleseismic arrivals and may be located on the Mendocino tranform fault [*Smith and Knapp*, 1980]. The August 17, 1991, M=6.2 Honeydew, California, earthquake, was located about 6 km south of the 1992 mainshock and had a similar focal mechanism, although there is some debate about whether the fault ruptured on the shallow dipping thrust plane or on the steeply dipping reverse fault [*Oppenheimer and Magee*, 1991;

[1]Now at Department of Geophysics, Stanford University, California.
[2]Also at Seismographic Station, University of California, Berkeley.
[3]Now at Trimble Navigation Ltd., Sunnyvale, California.
[4]Now at Hawaii Volcano Observatory, Hawaii National Park.

This paper is not subject to U.S. copyright. Published in 1996 by the American Geophysical Union.

Paper number 95JB02623.

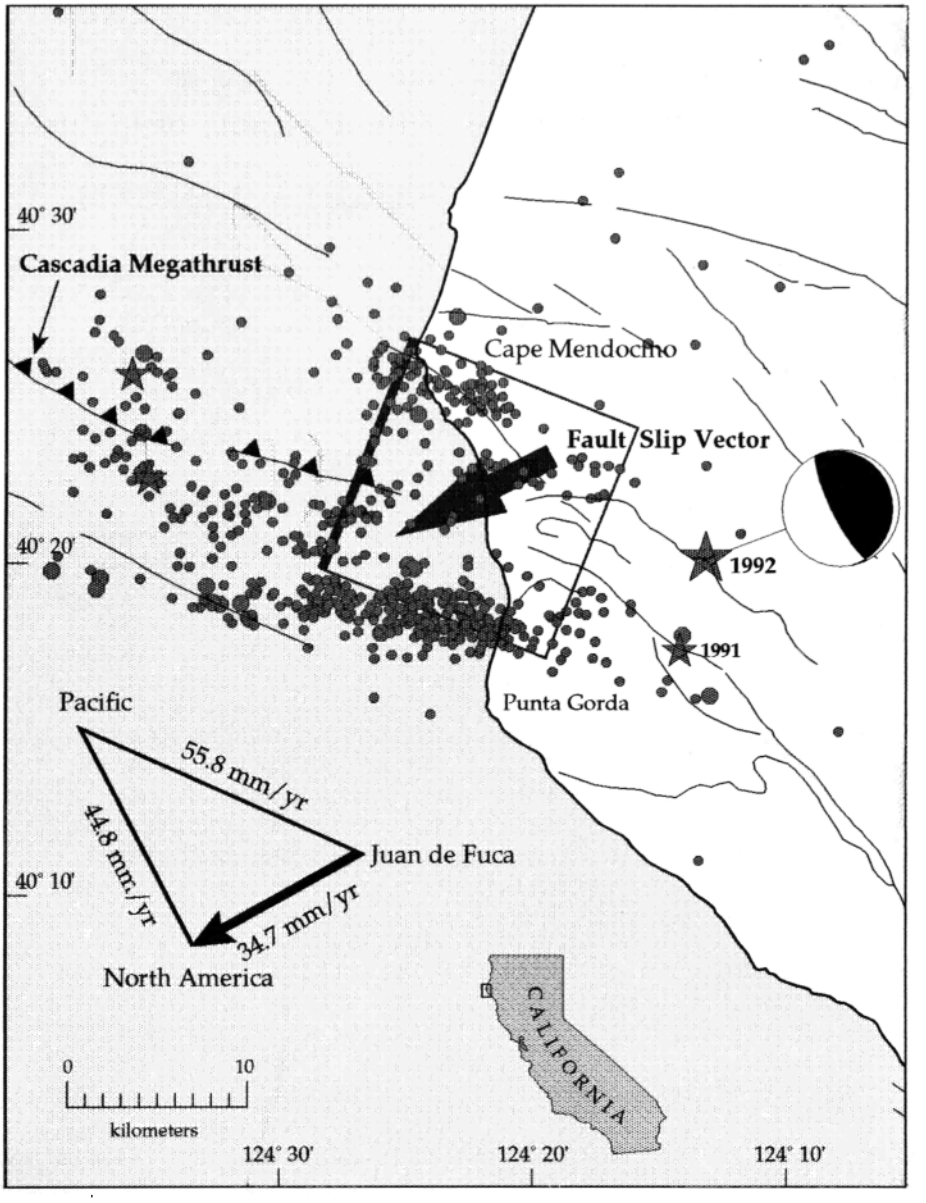

Figure 1. Epicentral region of the 1992 mainshock near Cape Mendocino, California. Large star, M=7 mainshock, with lower hemisphere focal mechanism (compression quadrants in black) derived from surface wave moment tensor analysis (strike=349.4°, dip=13.0°, rake=105.6°) [*Oppenheimer et al.*, 1993]. Smaller stars, epicenters of two M~6.6 aftershocks located offshore and 1991 M=6 Honeydew earthquake, located southeast of 1992 mainshock. Octagons, aftershock seismicity for 5-day interval after mainshock. Rectangle, surface projection of the SE-dipping thrust fault for one of the optimal models (model *A*, Table 7) derived from geodetic coseismic displacements. Large arrow in center of rectangle indicates direction of uniform slip vector projected to horizontal. Velocity diagram for relative motion between the Pacific, North America, and Juan de Fuca plates at approximate position of the Mendocino triple junction is shown in lower left-hand corner, with bold arrow indicating the rate of convergence of North America with respect to the Juan de Fuca plate. Southernmost mapped segment of the Cascadia megathrust, shown in bold with teeth on the upper plate, from *Clarke* [1992]. Other faults, here and in subsequent figures, modified from *Jennings* [1994], printed courtesy of California Department of Conservation, Division of Mines and Geology.

McPherson and Dengler, 1992]. Thus the Honeydew event may be associated with the Cascadia megathrust, or it may be associated with other structures, such as the nearby King Range.

The 1992 Cape Mendocino earthquake caused significant horizontal and vertical crustal deformation in the epicentral region. *Oppenheimer et al.* [1993] presented a dislocation model derived from coseismic displacements determined from Global Positioning System (GPS) and coastal uplift observations derived from the die-off of intertidal marine organisms [*Carver et al.*, 1994]. Here we use observations of horizontal interseismic deformation derived from 9 years of Geodolite trilateration measurements to correct the GPS coseismic displacements. We then present a revised dislocation model that includes leveling observations in addition to the GPS and coastal uplift observations. Because

the mainshock did not rupture the surface onshore, its fault location and geometry are primarily inferred from seismological observations. We use the geodetic observations to provide an independent estimate of the fault rupture. Finally, we compare the coseismic deformation caused by this earthquake with geologic estimates of deformation from studies of relative plate motions [*Wilson*, 1993] and from Holocene and Pleistocene marine terraces [e.g., *Merritts and Bull*, 1989] to estimate a recurrence interval of about 100–300 years for $M=7$ events at the south end of the Cascadia megathrust.

Geodetic Observations

Horizontal Interseismic Deformation

We estimate interseismic deformation in the Cape Mendocino area from the 18-station Mendocino trilateration network (Figure 2), surveyed 6 times during 1981–1989 by the U.S. Geological Survey (USGS). In 1989 the trilateration network was replaced by a 14-station GPS network (Figure 2), which has nine stations in common with or very near to stations in the trilateration network (Table 1). However, we cannot reliably estimate interseismic deformation from the

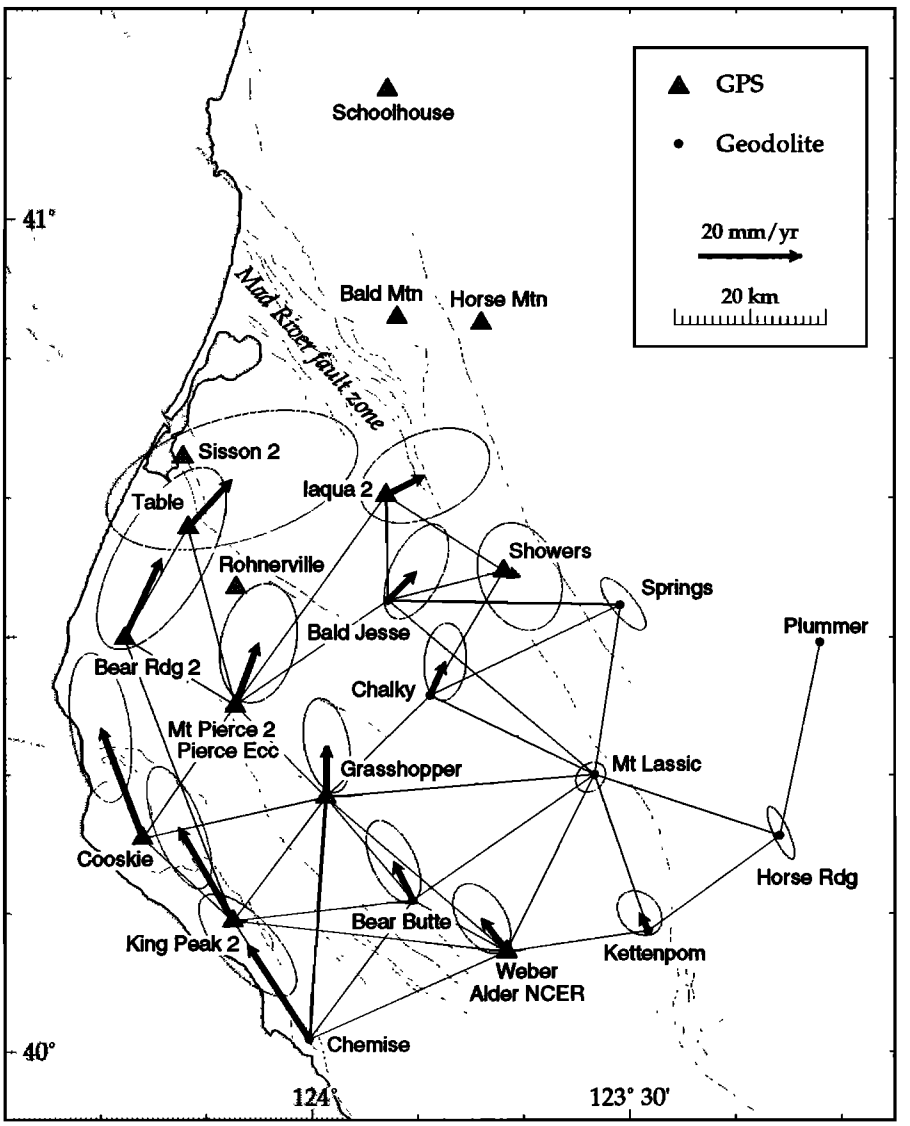

Figure 2. Cape Mendocino, California. Locations of stations in Geodolite trilateration network (circles) and Global Positioning System (GPS) network (triangles). Solid lines show distances measured between stations by Geodolite. Stations Bear Rdg 2, Cooskie, Grasshopper, Iaqua 2, King Peak 2, Showers, and Table are in both networks; GPS stations Pierce Ecc and Alder are collocated with nearby Geodolite stations Mt Pierce 2 and Weber, respectively. Average horizontal station velocities (arrows) determined from Geodolite measurements made between 1981 and 1990. Error ellipses represent 95% confidence regions. Velocities are relative to stations Springs, Horse Rdg, and Mt Lassic in eastern part of network, whose root-mean-square (rms) velocities were minimized to resolve the rigid body motion of the network.

Table 1. Geodolite and GPS Stations

Station	Geodolite	GPS	Latitude, ° N			Longitude, ° W			Velocity, mm/yr		Sigma, mm/yr		East-North Correlation
									East	North	East	North	
Alder NCER		×	40	7	13.033	123	41	35.413	–4.9	6.5	2.3	2.8	–0.447[a]
Bald Mtn		×	40	52	55.224	123	51	55.453	0.0	0.0	0.0	0.0	0.000[b]
Bald Jesse	×		40	32	36.663	123	52	46.438	5.6	5.6	2.6	3.8	0.529
Bear Butte	×		40	10	54.861	123	50	26.927	–3.8	7.6	2.2	3.3	–0.519
Bear Rdg 2	×	×	40	29	51.726	124	17	40.139	7.3	15.7	5.2	7.3	0.645
Chalky	×		40	25	44.582	123	48	49.105	3.0	6.6	1.7	3.1	0.110
Chemise	×		40	0	50.241	124	0	16.306	–12.1	18.6	3.9	4.1	–0.694
Cooskie	×	×	40	15	24.531	124	15	57.662	–8.3	21.8	2.5	6.0	–0.318
Grasshopper	×	×	40	18	22.961	123	58	40.203	0.2	10.2	1.9	3.8	–0.300
Horse Mtn		×	40	52	28.997	123	43	58.608	0.0	0.0	0.0	0.0	0.000[b]
Horse Rdg	×		40	15	36.701	123	15	47.549	0.2	0.5	1.1	2.1	–0.797
Iaqua 2	×	×	40	40	8.290	123	52	57.438	7.7	3.9	5.2	3.8	0.371
Kettenpom	×		40	8	43.438	123	28	11.141	–1.8	3.4	1.8	1.8	–0.257
King Peak 2	×	×	40	9	24.611	124	7	27.426	–10.6	18.4	2.6	4.9	–0.628
Mt Lassic	×		40	20	2.216	123	33	16.063	–0.8	–0.6	1.2	1.2	0.233
Mt Pierce 2	×		40	25	2.000	124	7	13.991	4.6	12.2	3.1	4.8	0.209
Plummer	×		40	29	34.809	123	11	59.436	0.0	0.0	0.0	0.0	0.000[b]
Pierce Ecc		×	40	24	58.915	124	7	12.004	4.6	12.2	3.1	4.8	0.209[c]
Rohnerville		×	40	33	31.862	124	7	7.694	8.6	9.4	10.1	5.6	0.417[d]
Schoolhouse		×	41	9	12.264	123	52	55.030	0.0	0.0	0.0	0.0	0.000[b]
Showers	×	×	40	34	44.196	123	41	51.106	3.2	–1.2	3.4	4.3	–0.208
Sisson 2		×	40	42	55.568	124	12	7.098	8.6	9.4	10.1	5.6	0.417[d]
Springs	×		40	32	17.227	123	30	50.160	0.6	0.1	1.8	2.1	–0.775
Table	×	×	40	37	49.056	124	11	37.389	8.6	9.4	10.1	5.6	0.417
Weber	×		40	7	12.391	123	41	35.208	–4.9	6.5	2.3	2.8	–0.447

[a] Velocity assumed equal to velocity of nearby station Weber.
[b] Insufficient data to estimate velocity, velocity assumed equal to zero.
[c] Velocity assumed equal to velocity of nearby station Mt Pierce 2.
[d] Velocity assumed equal to velocity of nearby station Table.

GPS observations made since 1989 due to possible displacements caused by the 1991 Honeydew and 1992 Cape Mendocino earthquakes. Therefore we use the interseismic deformation inferred from the trilateration measurements to correct the coseismic displacements derived from GPS measurements that span several years.

Distances in the Mendocino trilateration network were measured with a Geodolite, a precise electro-optical distance-measuring instrument. The refractivity correction was calculated from endpoint pressure measurements and from temperature and humidity profiles measured by a small aircraft flying along the line at the time of ranging. The standard error in the measurement is $\sigma = (a^2 + b^2L^2)^{1/2}$, where a = 3 mm, b = 0.2 ppm, and L is the distance measured [*Savage and Prescott*, 1973; *Savage et al.*, 1986]. The standard error of the average line length (24.4 km) is 5.7 mm. A linear rate of change provides a reasonable fit to the data for each of the 38 lines in the network. Of the 171 distance measurements, only 22 lie more than 1 standard error from the linear fit, which is better than expected for a normal distribution of measurement error.

The average velocities of the stations in the Mendocino network (Table 1) were calculated by a variation-of-coordinates procedure [*Bomford*, 1980, pp. 126–144], using the linear rates of change in line length. The rigid body motion of the network, which is unconstrained by trilateration observations, was resolved by selecting the solution with the minimum root-mean-square (rms) velocity for a subset of stations [*Prescott*, 1981; *Gu and Prescott*, 1986]. We selected three stations (Springs, Mt Lassic, and Horse Rdg, Figure 2) in the eastern part of the network where the lowest strain rates in the Mendocino network were observed.

The average station velocities show a transition from right-lateral shear south of Cape Mendocino to northeast directed uniaxial contraction north of Cape Mendocino (Figure 2). The relative velocities of stations in the southern part of the network decrease to the east and are oriented parallel to the San Andreas fault system. The total right-lateral strike-slip deformation accommodated across this zone is about 25 mm/yr, or 65% of the 38 mm/yr of relative motion observed across the San Andreas fault system in the San Francisco Bay region [*Lisowski et al.*, 1991]. The relative velocities of stations north of Cape Mendocino change to northeastward orientation and decrease to the north. These relative motions are consistent with about 15 mm/yr northeastward directed uniaxial contraction from Cape Mendocino to north of the Mad River fault zone. This rate agrees with geologic estimates of deformation across the region, which is thought to be a fold-and-thrust belt formed within the forearc immediately landward of the Cascadia subduction zone [*Kelsey and Carver*, 1988].

GPS Observations

The relative displacements between 14 geodetic monuments within 100 km of Cape Mendocino (Figure 2) were determined from four GPS surveys conducted by the USGS in 1989, 1991, and 1992 (Table 2). The GPS observations were analyzed with the Bernese software package using methods described by *Davis et al.* [1989]. Orbits were improved using observations from fiducial GPS receivers operated by the U.S. National Geodetic Survey (NGS) in Mojave, California, Richmond, Florida, and Westford, Massachusetts. Orbital parameters,

Table 2. GPS Coseismic Displacements

Station	Occupations				Displacement, mm			Sigma, mm			East-North Correlation
	May 1989	July 1989	Oct. 1991	May 1992	East	North	Up	East	North	Up	
Alder NCER	O		U	U	-3.0	25.3	2	4.6	5.1	38	-0.3269
Bald Mtn	U			U	-16.4	-3.9	16	4.8	4.5	29	0.0124
Bear Rdg 2		O	U	U	-197.3	-113.9	-61	5.2	7.6	43	-0.1739
Cooskie	O		U	U	-82.3	-92.0	63	4.5	4.8	35	-0.3562
Grasshopper	O		U	U	-128.8	52.6	-36	4.6	5.0	37	-0.3354
Horse Mtn	U			U	-11.8	-4.3	-20	6.1	6.0	36	-0.2771
Iaqua 2	U			U	-55.8	-31.6	6	3.5	3.4	22	-0.0159
King Peak 2	O		U	U	-18.4	56.3	20	5.0	5.4	40	-0.3515
Pierce Ecc		U		U	-386.7	-64.8	-158	11.3	9.5	81	0.0833
Rohnerville	U			U	-126.8	-110.1	-15	4.3	4.0	27	0.0542
Schoolhouse[a]	U			U	0.0	0.0	0	0.0	0.0	0	0.0000
Showers	U			U	-59.5	-14.1	-22	4.5	4.4	29	-0.0737
Sisson 2	U			U	-22.7	-36.4	11	4.2	4.0	27	0.0424
Table	O	O	U	U	-17.6	-48.1	16	4.8	4.4	27	-0.0647

U, Used to derive coseismic displacement.
O, Observed but not used to determine coseismic displacement.
[a] Velocity assumed equal to zero.

relative station locations, atmospheric zenith delay parameters, and doubly differenced carrier-phase ambiguities were estimated from the ionosphere-free linear combination of the L1 and L2 carrier phase observations. The ambiguities were resolved to integer values whenever their real-valued estimates had an uncertainty less than 0.05 cycle and differed from an integer by less than 3 times their uncertainty. Most ambiguities were resolved for baselines within the Cape Mendocino network. The uncertainties in the relative station vectors based on the scatter of day-to-day measurements during each survey are about 5–10 mm in the horizontal and 30 mm in the vertical components, which are typical values for GPS surveys conducted in California [e.g., *Davis et al.*, 1989].

Each three-dimensional coseismic GPS displacement is determined by subtracting a preseismic position observed in either 1989 or 1991 from the postseismic position of the station observed in May 1992 (Table 2). We subtracted position vectors relative to the station Table, which was observed in all the surveys, and propagated the relative position covariance. If the station was observed more than once before 1992, we use the most recent preseismic survey to minimize the effects of interseismic deformation and of coseismic displacements caused by the 1991 Honeydew earthquake, which occurred 6 km south of the 1992 Cape Mendocino epicenter. The positions of 6 stations were measured soon after the Honeydew earthquake. The displacements predicted by a focal mechanism determined University of California, Berkeley for the Honeydew event (L. Gee, personal communication, 1993) indicate that the other GPS stations moved less than 15 mm, except for Pierce Ecc, which may have moved 50 mm. Because absolute station positions (i.e., with respect to the fiducial network) are not well determined by these surveys, all relative displacements are translated and their covariances propagated so that Schoolhouse, the station most distant from the mainshock, did not move. For each station we then subtract the horizontal interseismic deformation predicted for the interval between the preseismic and postseismic surveys, using the rates measured by Geodolite trilateration during 1981–1989 (Table 1). The corrections, which we assumed were without error, are all less than 40 mm.

The coseismic displacements determined by GPS are given in Table 2 and shown in Figure 3. Most of the horizontal displacements are greater than their measurement uncertainties. The largest measured horizontal displacement is 400±20 mm at station Pierce Ecc, which is much greater than the 50-mm coseismic displacement predicted for the Honeydew earthquake, suggesting that possible uncorrected effects due to the Honeydew earthquake are not significant. The three stations closest to the mainshock epicenter (Pierce Ecc, Cooskie, and Bear Rdg 2) were also vertically displaced greater than their measurement uncertainty (Figure 3).

Leveling Observations

Vertical deformation associated with the 1992 Cape Mendocino earthquake was also measured from leveling surveys. Spirit leveling measures the height between adjacent bench marks (BMs), or section-elevation differences. Coseismic observations are derived by subtracting section-elevation differences measured before the earthquake, during the interval 1935–1988, from section-elevation differences measured in a survey conducted by NGS leveling crews after the earthquake, during the interval August–October 1992. The leveling network encompasses the epicentral regions of the 1991 Honeydew and 1992 Cape Mendocino earthquakes and is divided into four routes corresponding to the NGS job number in 1992 (Figure 4).

Interseismic vertical deformation can be inferred only along route 1 (Figure 4), which was leveled in 1967 and 1988. These surveys have 75 BMs in common providing a measure of the vertical movement of the water-saturated sedimentary deposits of the Eel River basin between 1967 and 1988. The vertical movement measured in the interval 1967–1988 is used to correct circuit misclosures and the coseismic displacements along route 1 (see Appendix). Routes 2, 3, and 4 were each surveyed only once before the earthquake in 1935 or 1942, and therefore provide no information about interseismic motions of the BMs during the ~50 years preceding the 1992 earthquake.

Survey precision is assessed by analysis of the double-run sections (multiple observations of the height between

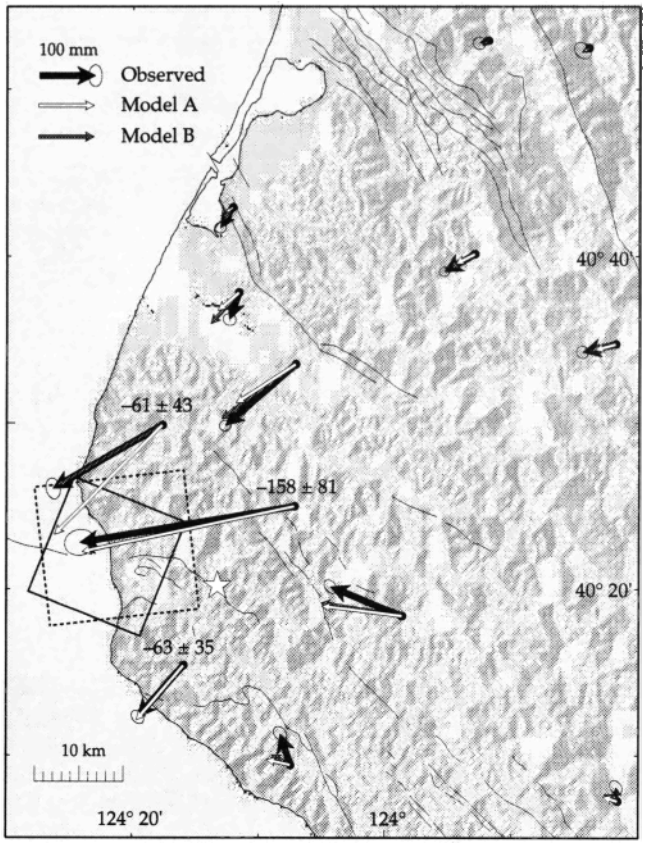

Figure 3. Cape Mendocino, California, showing observed (solid arrows) and predicted (open arrows, model *A*; gray arrows, model *B*) horizontal coseismic displacements from Global Positioning System measurements. Error ellipses represent 95% confidence regions. Displacements are with respect to station Schoolhouse (see Figure 2). Rectangle, optimal fault plane projected to the surface (solid, model *A*; dashed, model *B*). Star, 1992 M=7 Cape Mendocino mainshock.

adjacent BMs). Specifications and double-run section precision estimates ($\alpha_{F\text{-}B}$) for each survey are listed in Table 3. One standard error is $\alpha_{F\text{-}B}$ = ~1.33 mm/km$^{1/2}$ for first order, class II, and ~2.67 mm/km$^{1/2}$ for second order levels, assuming field tolerances of 4 and 8 mm, respectively. All but one survey (L4576) have precision within 1 standard error, although some of the surveys have too few double-run sections to accurately assess their precision.

We examine both systematic and random errors for each of the four leveling routes. No significant systematic errors were detected by tests for slope-dependent height changes associated with miscalibrated leveling rods [*Stein*, 1981], and no magnetic compensator errors typical to leveling conducted between 1967 and 1988 with Zeiss Ni1 automatic compensators [*Ekström et al.*, 1992] were found in the 1967 and 1988 surveys. Random errors are estimated from both circuit misclosures and double-run sections, and each survey is assigned a precision based on this analysis (see Appendix). All postseismic surveys are assigned a precision of α_{post} = 0.96 mm/km$^{1/2}$; the preseismic survey of route 1 is assigned α_{pre} = 0.80 mm/km$^{1/2}$, and routes 2, 3, and 4 are assigned α_{pre} = 1.90 mm/km$^{1/2}$. An uncertainty is given to each section's coseismic elevation change that is dependent on the survey precision, the length of the section, and any applied subsidence correction:

$$\sigma = \sqrt{(\alpha\sqrt{L})^2 + (0.5\ S)^2} \quad (1)$$

where $\alpha = \sqrt{\alpha_{pre}^2 + \alpha_{post}^2}$ represents the combined survey precision of the pre-earthquake and postearthquake leveling, L is the length of the section (in kilometers), and S is the subsidence correction for that section. We arbitrarily inflate the error by one half the subsidence in (1) to reflect the mean uncertainty of estimating the subsidence. We assume that the section-elevation differences are uncorrelated. Leveling section-elevation differences measure the relative deformation between benchmarks, rather than absolute height differences. We assume that the section-elevation differences are uncorrelated, which is essentially equivalent to using height differences with correlations derived following *Árnadóttir et al.* [1992].

Coseismic section-elevation changes and their associated section lengths and uncertainties are listed in Table 4. Profiles of the change in elevation along each route, relative to an arbitrary datum, are shown in Figure 5. The most significant changes in elevation were measured at two benchmarks (LV0368 and LV0369) located on the coast along route 3 that

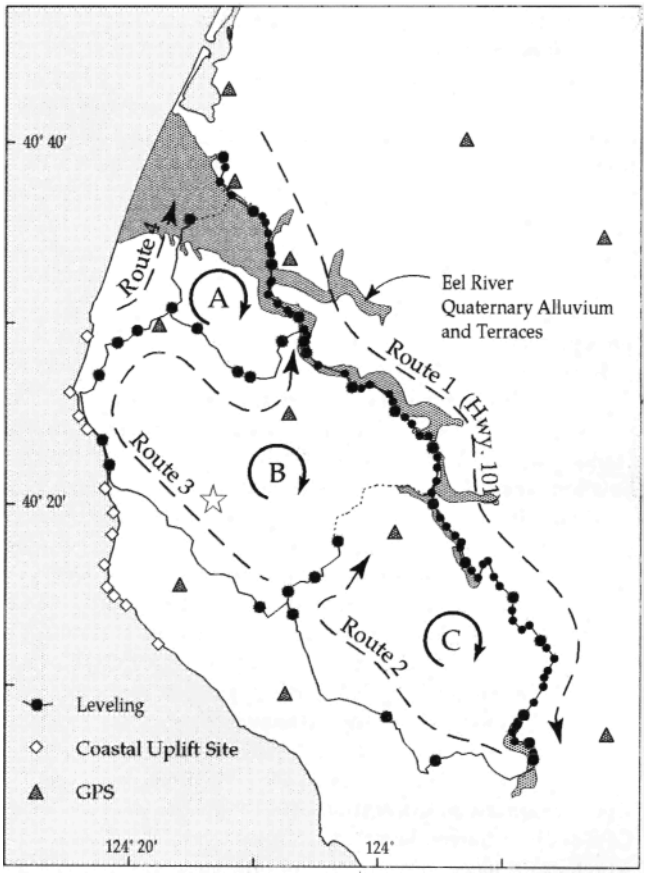

Figure 4. Cape Mendocino, California, showing leveling bench marks used to determine coseismic elevation changes (solid circles) and coastal locations where intertidal marine organism die-off was measured (open diamonds). The larger solid circles were used to test the effect of decimating the route 1 data. Four leveling routes are labeled, indicating increasing distance along leveling profiles. Circuit closures are calculated for Loops A, B, and C. Loop A+B+C is the larger outer loop. Dashed region is the Eel River basin and terraces, composed of Quaternary alluvium deposits, from *Strand* [1962]. Star, 1992 M=7 Cape Mendocino mainshock.

Table 3. Leveling Specifications

Route	L Number[a]	Date	Order, Class	$\alpha_{F\text{-}B}$[b] mm/√km	Double-Run, count/%
			Preseismic Data		
1	L389	Nov. 1931	1,II	1.32	794/99
1	L21206	Aug. 1967	1,II	1.35	702/100
1	L25053	Oct. 1988	1,II	0.80	49/20
2	L4576	Feb. 1935	2	3.48	2/4
2	L6711/2	June 1935	2	2.03	2/2
2,3,4	L5479	Jan. 1935	2	2.18	20/2
3	L6711/1	June 1935	2	n/a[c]	0/0
3	L9851	June 1942	2	2.22	8/33
			Postseismic Data		
1	L25377/1	Aug. 1992	1,II	1.21	9/10
2	L25377/2	Sept. 1992	1,II	1.16	10/11
3	L25377/3	Oct. 1992	1,II	0.85	8/11
4	L25377/4	Oct. 1992	1,II	0.93	2/10

[a]L number is the leveling job reference number used by the National Geodetic Survey.

[b]Variable $\alpha_{F\text{-}B} = \frac{1}{N}\sum_{j}^{N}\sqrt{\mathrm{var}_j D_j}$, where $\mathrm{var}_j = \frac{1}{n_j}\sum_{i}^{n_j}(h_i - h_{\mathrm{ave}})^2$, N is the number of double-run sections, D_j is the length (in kilometers) of the jth double-run section, n_j is the number of runnings of the jth double-run section, h_i is the observed height of the section (in millimeters), and h_{ave} is the average height of the n_j runnings.

[c]Abbreviation n/a, not applicable.

were uplifted 0.8–1.0 m relative to other benchmarks in the same route (Figure 5b). Modest subsidence of ~0.07 m occurred along route 1 in the eastern part of the leveling network (Figure 5c).

Coastal Uplift Observations

The uplift of the Mendocino coastline killed marine intertidal flora and fauna that are sensitive to height above sea level. To estimate the coseismic elevation change, *Carver et al.* [1994] measured the vertical extent of the death of species affixed to coastal outcrops. Mussels, barnacles, and seaweed (*Pelvetoipsis*) at 12 coastal sites were the most reliable indicators of coastal uplift (Figure 4). At each site, we use the mean height change estimated from the three marine intertidal indicators, assigning half the difference in elevation change measured for the mussels and seaweed as the measurement uncertainty. Where only one species was present, we used the mean uncertainty of the redundant observations, 150 mm (Table 5). Each coastal marine observation is an independent measurement of elevation change relative to a common reference datum (sea level), in contrast to the leveling observations that measure relative deformation between BMs and have an arbitrary datum.

The coastal uplift observations indicate that the coast between Cape Mendocino and Punta Gorda was uplifted about 1 m (Figure 5a), in agreement with the two leveling BMs located near the coast. North of Cape Mendocino and 5 km south of Punta Gorda no reliable indicators of coastal uplift were found, although a few coastal outcrops suggest that little or no uplift occurred.

Dislocation Modeling

Optimal Models

We use the coseismic surface displacements derived from GPS, leveling, and coastal uplift observations to infer the

Table 4. Leveling Benchmarks and Elevation Differences

ACRN[a]	Latitude, °N	Longitude, °W	Elevation Change,[b] mm	Subsidence Correction, mm	Section[c] Distance, km	Section[c] Elevation Difference, mm	Section[c] Error, mm
			Route 1; α = 1.25; Coseismic Interval 1992–1988				
LV0250	40.6519	124.2100	−2.33	−14.24			
LV0248	40.6425	124.2075	−23.70	−10.94	1.25	2.37	2.16
LV0659	40.6294	124.2144	−125.44	−10.43	1.51	1.74	1.56
LV0243	40.6172	124.1986	−32.84	−9.67	2.25	7.40	1.91
LV0239	40.6019	124.1692	−31.92	−8.45	3.59	−0.92	2.45
LV0238	40.5975	124.1575	−34.30	−8.03	1.07	2.38	1.31
LV0237	40.5922	124.1533	−33.53	−7.14	1.02	−0.77	1.34
LV0236	40.5822	124.1497	−42.09	−6.19	1.21	8.56	1.46
LV0234	40.5708	124.1481	−48.68	−5.99	1.37	6.59	1.47
LV0235	40.5692	124.1464	−48.50	−5.79	0.15	−0.18	0.50
LV0660	40.5633	124.1453	−50.55	−5.09	0.53	2.05	0.97
LV0233	40.5536	124.1444	−55.04	−3.49	1.20	4.49	1.59
LV0231	40.5386	124.1447	−58.70	−0.27	1.61	3.66	2.26
LV0664	40.5367	124.1467	−59.06	0.22	0.25	0.36	0.67
LV0229	40.5261	124.1497	−62.48	2.80	1.31	3.42	1.93
LV0665	40.5178	124.1369	−63.31	3.03	1.34	0.83	1.45
LV0666	40.5117	124.1233	−75.03	3.27	1.38	11.72	1.47
LV0667	40.5083	124.1189	−75.69	3.36	0.54	0.66	0.92
LV0668	40.5055	124.1083	−68.70	3.53	0.95	−6.99	1.22
LV0395	40.4945	124.1011	−69.33	4.00	2.75	0.63	2.09
LV0669	40.4886	124.0975	−69.69	4.52	0.48	0.36	0.90
LV0393	40.4831	124.1011	−72.98	5.35	0.77	3.29	1.17
LV0670	40.4728	124.0983	−73.76	4.39	1.16	0.78	1.43
LV0671	40.4614	124.0828	−74.33	2.71	2.01	0.57	1.96
LV0673	40.4539	124.0467	−68.91	0.00	3.25	−5.42	2.63
LV0430	40.4414	124.0364	−67.11	−1.43	1.71	−1.80	1.78
LV0429	40.4403	124.0250	−58.77	−1.11	1.07	−8.34	1.30
LV0428	40.4439	124.0133	−61.39	−3.56	0.96	2.62	1.73
LU1490	40.4350	123.9869	−47.01	−2.74	2.65	−14.38	2.08
LU1489	40.4281	123.9822	−39.91	−0.32	0.90	−7.10	1.69
LU1875	40.4192	123.9794	−40.52	−0.17	0.91	0.61	1.20
LU1487	40.4139	123.9664	−32.72	0.07	1.49	−7.80	1.53
LU1486	40.4078	123.9572	−28.54	0.09	1.12	−4.18	1.33
LU1485	40.3972	123.9464	−33.70	−2.62	1.48	5.16	2.04
LU1484	40.3969	123.9347	−26.88	−0.52	0.82	−6.82	1.54
LU1876	40.3864	123.9292	−28.50	−2.78	1.37	1.62	1.85
LU1482	40.3769	123.9236	−34.27	−4.65	1.14	5.77	1.63
LU1481	40.3678	123.9233	−30.50	−1.74	1.13	−3.77	1.97
LU1877	40.3553	123.9242	−26.65	−2.25	1.71	−3.85	1.65
LU1310	40.3447	123.9308	−25.53	−2.72	1.61	−1.12	1.60
LU1309	40.3344	123.9286	−20.70	−0.67	1.34	−4.83	1.77
LU1307	40.3217	123.9200	−20.26	−2.03	1.65	−0.44	1.74
LU1306	40.3136	123.9108	−13.51	−1.83	1.35	−6.75	1.46
LU1304	40.3053	123.8997	−17.33	−5.03	1.30	3.82	2.14
LU1303	40.2992	123.8908	−7.43	−1.90	1.15	−9.90	2.06
LU1302	40.2942	123.8925	−12.17	−2.39	0.58	4.74	0.98
LU1299	40.2808	123.8855	−6.06	−3.87	2.00	−6.11	1.92
LU1298	40.2733	123.8775	−5.93	−5.83	1.09	−0.13	1.63
LU1295	40.2667	123.8683	−7.45	−4.14	1.13	1.52	1.57
LU1293	40.2792	123.8617	−7.61	−5.44	1.64	0.16	1.73
LU1292	40.2822	123.8555	−10.15	−6.06	0.80	2.54	1.16
LU1290	40.2678	123.8472	−9.04	−5.55	1.88	−1.11	1.73
LU1289	40.2592	123.8394	−9.17	−6.90	1.15	0.13	1.50
LU1286	40.2492	123.8217	−6.62	−5.11	2.59	−2.55	2.20
LU1284	40.2370	123.8228	−8.04	−3.35	1.37	1.42	1.71
LU1879	40.2278	123.8217	−11.17	−3.60	1.19	3.13	1.37
LU1280	40.2194	123.8097	−14.83	−3.95	1.66	3.66	1.62
LU1279	40.2233	123.7997	−8.98	−3.98	1.03	−5.85	1.27
LU1275	40.2097	123.7845	−8.44	−4.51	2.65	−0.54	2.05
LU1274	40.2033	123.7767	−10.66	−3.44	1.03	2.22	1.38
LU1272	40.1931	123.7661	−12.18	−3.29	1.60	1.52	1.58
LU1271	40.1820	123.7747	−13.01	−2.67	1.57	0.83	1.60
LU1880	40.1758	123.7800	−11.52	−4.57	0.79	−1.49	1.46
LU1270	40.1678	123.7806	−13.55	−6.83	0.94	2.03	1.66
LU1881	40.1528	123.7936	−9.43	−5.97	2.14	−4.12	1.88
LU1267	40.1419	123.8067	−5.17	−5.28	1.73	−4.26	1.68

Table 4. (continued)

ACRN[a]	Latitude, °N	Longitude, °W	Elevation Change,[b] mm	Subsidence Correction, mm	Section[c] Distance, km	Section[c] Elevation Difference, mm	Section[c] Error, mm
LU1266	40.1356	123.8142	-5.59	-2.72	0.90	0.42	1.74
LU1265	40.1314	123.8164	-2.57	-0.83	0.55	-3.02	1.32
LU1264	40.1261	123.8220	-0.89	1.79	0.81	-1.68	1.72
LU1882	40.1172	123.8186	-2.84	0.70	1.16	1.95	1.45
LU1262	40.1164	123.7992	-1.20	-0.91	1.72	-1.64	1.83
LU1259	40.1067	123.7939	0.06	-0.38	1.48	-1.26	1.54
LU1257	40.1058	123.7942	0.88	0.32	0.11	-0.82	0.54
LU1255	40.1011	123.7936	1.23	1.03	0.55	-0.35	0.99
LU1254	40.0997	123.7953	0.00	-1.69	0.30	1.23	1.52
Route 2; α = 2.13; Coseismic Interval 1992–1935							
LU1262	40.1164	123.7992	-1.20	-0.91			
LU1472	40.1000	123.9242	10.79	0.00	20.72[d]	-11.99	9.69
LU1477	40.1397	123.9897	37.95	0.00	13.13	-27.16	7.72
LV0382[e]	40.2328	124.1153	149.92	0.00	20.79	-111.97	9.71
LV0427[e]	40.2536	124.1222	124.76	0.00	3.43	25.16	3.94
LV0425[e]	40.2667	124.0864	56.50	0.00	5.71	68.26	5.09
LV0423[e]	40.2997	124.0558	-13.58	0.00	6.90	70.08	5.60
Route 3; α = 2.13; Coseismic Interval 1992–1935, 1942							
LV0382	40.2328	124.1153	68.90	0.00			
LV0379	40.2392	124.1595	47.81	0.00	5.86	21.09	5.15
LV0369	40.3692	124.3611	818.72	0.00	28.25	-770.91	11.32
LV0368	40.3922	124.3703	735.32	0.00	2.75	83.40	3.53
LV0365	40.4517	124.3747	-282.97	0.00	9.30	1018.29	6.49
LV0363	40.4817	124.3503	-114.96	0.00	6.28	-168.01	5.34
LV0362	40.4928	124.3239	-227.53	0.00	3.15	112.57	3.78
LV0410	40.4950	124.2442	-198.30	0.00	9.67	-29.23	6.62
LV0405	40.4553	124.1897	-189.05	0.00	7.09	-9.25	5.67
LV0404	40.4503	124.1728	-150.43	0.00	1.52	-38.62	2.63
LV0399	40.4833	124.1305	-69.95	0.00	7.68	-80.48	5.90
LV0393	40.4831	124.1011	-72.98	5.35	4.29[d]	3.03	4.41
Route 4; α = 2.13; Coseismic Interval 1992–1935							
LV0362	40.4928	124.3239	-227.53	0.00			
LV0220	40.5136	124.2775	-113.56	0.00	6.33	-113.97	5.36
LV0217[e]	40.5947	124.2536	-268.60	0.00	11.92	155.04	7.35

[a]Archival reference number used by National Geodetic Survey to uniquely identify each benchmark independent of the stamped designation.

[b]Relative to benchmark LU1254, the benchmark farthest from the earthquake source. An arbitrary constant may be added to all elevation changes. Subsidence corrections are not applied to the listed elevation changes.

[c]Section is from the preceding benchmark in list to the benchmark.

[d]Subsidence correction not used to estimate error.

[e]Benchmark disturbed or unstable (motion not due to the Cape Mendocino earthquake), determined by inspection.

fault geometry and slip for the 1992 Cape Mendocino earthquake. We assume the fault is a rectangular dislocation embedded in a homogeneous, elastic, isotropic half-space with its top edge parallel to the surface, and the slip across this fault is constant. The surface vector displacements, **d**, caused by an elastic dislocation on a buried fault are nonlinear functions of the seven parameters describing the rectangular fault geometry, **m** (the three-dimensional location, dip, strike, along-strike length, and downdip width), and linear functions of the slip vector, **u**:

$$\mathbf{d} = \mathbf{G}(\mathbf{m})\,\mathbf{u} \tag{2}$$

where the matrix $\mathbf{G}(\mathbf{m})$ incorporates the nonlinear geometric relationships given by *Okada* [1985]. We assume the mechanism is a pure double couple, therefore **u** can be expressed by its dip-slip and strike-slip components or, equivalently, by its magnitude and rake.

We assume the optimal fault geometry and slip minimizes the misfit between the observed and theoretical displacements given by the minimization function:

$$\chi^2 = \mathbf{r}^T \mathbf{C}^{-1}\,\mathbf{r} \tag{3}$$

that is, the sum of the squares of the residuals, $\mathbf{r} = \mathbf{d} - \mathbf{G}(\mathbf{m})\,\mathbf{u}$, weighted by the data covariance, **C**. When the fault geometry **m** is known, linear least squares inversion techniques can be used to estimate the optimal slip **u** that minimizes χ^2. However, more sophisticated techniques must be used if both the fault geometry and slip are estimated. These techniques must be able to accommodate the nonlinear relationships expressed by $\mathbf{G}(\mathbf{m})$, and to find the global minimum in the presence of multiple local minima. χ^2 has a local minimum associated with each of the auxiliary planes of the double-couple mechanism, but it can also have other local minima associated with models that, for example, decrease the misfit at particular stations. We have found that global optimization methods using Monte Carlo simulations are suitable for these types of problems.

Monte Carlo optimization techniques start by choosing, often by a random process, a trial model $(\mathbf{m}, \mathbf{u})_i$ from the set of all possible models *S*, and then determining the misfit to the data predicted by the trial model by forward calculation [e.g., *Press*, 1968]. This process is repeated using different trial models until a minimum misfit is found. Because only forward calculations are required, Monte Carlo simulations can accommodate nonlinear relationships between the data and model parameters, but they also can be computationally intensive. The easiest ways to choose trial models are by evaluating a regular grid of model parameters that spans *S*, and by pure random sampling, which randomly choses the model parameters from a uniform distribution over *S*. Although pure random sampling is more efficient than grid search at sampling *S*, both can require a prohibitively large number of trials to be evaluated in order to locate the global minimum with sufficient precision.

Several global optimization techniques have recently been developed that are significantly more efficient than pure random sampling. Simulated annealing, the first of these techniques to be widely used, is a method inspired by the physical annealing of solids by slow cooling to a state of minimum energy [*Kirkpatrick et al.*, 1983]. However, it is not particularly simple to implement because a cooling schedule appropriate for each problem must be devised. Other techniques, such as genetic algorithms [*Holland*, 1992] and taboo search [*Cvijovic and Klinowski*, 1995], are more straightforward. Here we use the random-cost optimization approach [*Berg*, 1993], which is easy to implement and theoretically guaranteed to find the global minima. It can also be highly efficient. *Berg* [1993] estimated random-cost optimization to be 10^{11} faster than pure random sampling at finding the extrema of a simple function, and *Wang et al.* [1994] found it to be 5–10 times faster than simulated annealing at solving a problem in genetics.

The random-cost approach begins by generating a set of trial models that span a region of *S* about an a priori model. We follow *Berg* [1993] by defining a grid in parameter space by geometric progressions; that is, for each trial model all the parameters are set equal to the a priori model except for one

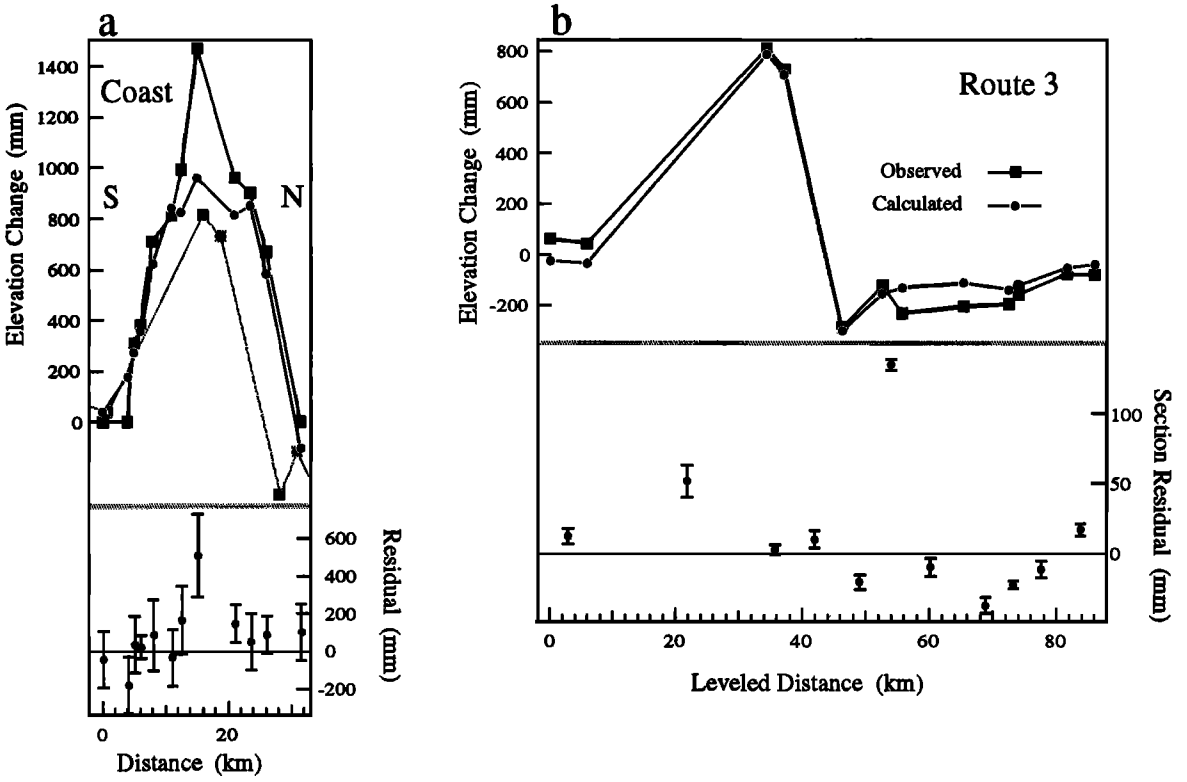

Figure 5. Observed and predicted elevation changes as a function of distance along profiles. Coastal uplift elevation changes are shown in Figure 5a. Leveling section difference observations and derived profiles for four routes (see Figure 4) are shown in Figures 5b–5e. Bottom of each leveling plot shows section difference residuals with respect to predicted using model A, 1 standard deviation error bars. Top of each leveling plot shows derived elevation change profiles, arbitrarily offset to show approximate misfit. Coast uplift plot is similar to leveling uplift plots, except that elevation change residuals and profiles with respect to mean sea level are shown. Observations with slashed circle in Figures 5d and 5e were omitted from model estimate because of possible effects from the 1991 Honeydew earthquake or from groundwater withdrawal-induced subsidence.

parameter m, whose grid locations are derived from $m_i = m_o \pm 2^{-i}\Delta m$ where m_o is the a priori value, i is an integer controlling the spacing of the grid near m_o, and Δm specifies the range of the parameter to be sampled, which is maximum when $i = 0$. This procedure for generating the trial models is not unique. However, by choosing Δm to be a large fraction of the total range of m (e.g., 50%), the models sample a sufficiently broad region of S to avoid being trapped in a local minimum. We typically let i range from 0 to 15, which makes the grid sufficiently dense near the a priori model to obtain the desired parameter precision.

For each trial model, the χ_i^2 (which Berg calls the cost function) is evaluated and compared to the a priori model χ_o^2. In general, the "cost difference" $\Delta\chi^2 = \chi_i^2 - \chi_o^2$ is either negative ($\Delta^-\chi^2$) or positive ($\Delta^+\chi^2$) depending on whether the trial model is better or worse than the a priori model, respectively. Let f^- equal the average $\Delta^-\chi^2$ of all the better trial models and f^+ be similarly derived from all the worse trial models, and let $P^- = f^+/(f^+ - f^-)$ and $P^+ = 1 - P^-$. A new a priori model is randomly selected from either the set of better or worse trial models according to the probabilities $P^{\pm}$; by sometimes choosing a worse trial model, the procedure can avoid being trapped in a local minimum. The process is repeated until a local minimum (or maximum) is encountered; that is, until no better (or worse) trial models are found. This minimax model is recorded and then the process is restarted at another randomly chosen a priori model. By using the probabilities $P^{\pm}$ at each iteration to determine the new a priori model, a random walk in the minimization function χ^2 space (rather than in the parameter space S) is enforced, which ensures that local minima will be found within a finite number of steps [*Berg*, 1993].

We modify this basic random-cost approach to take advantage of the linear relationship between surface displacements and fault slip (equation (2)). We create trial models by varying the seven parameters that describe the fault geometry, making weak assumptions on the range of parameters, such as high upper bounds on location and fault dimensions and obvious nonnegative constraints on width, length, and top edge depth. Then for each trial geometry we use least squares techniques to estimate the slip vector that minimizes χ^2. In practice, we found that the random walk usually descends the minimization function and converges on local minima, but occasionally it ascends to where it might encounter another local minima. We also found that the convergence was relatively slow if the desired precision was high (e.g., $i = 15$). On the other hand, iterative nonlinear inversion techniques, such as quasi-Newton methods [e.g., *Árnadóttir and Segall*, 1994], can rapidly converge on a local, but not necessarily global, minimum. This suggests that a hybrid method using the random-cost approach to locate regions with local minima and then using nonlinear inversion

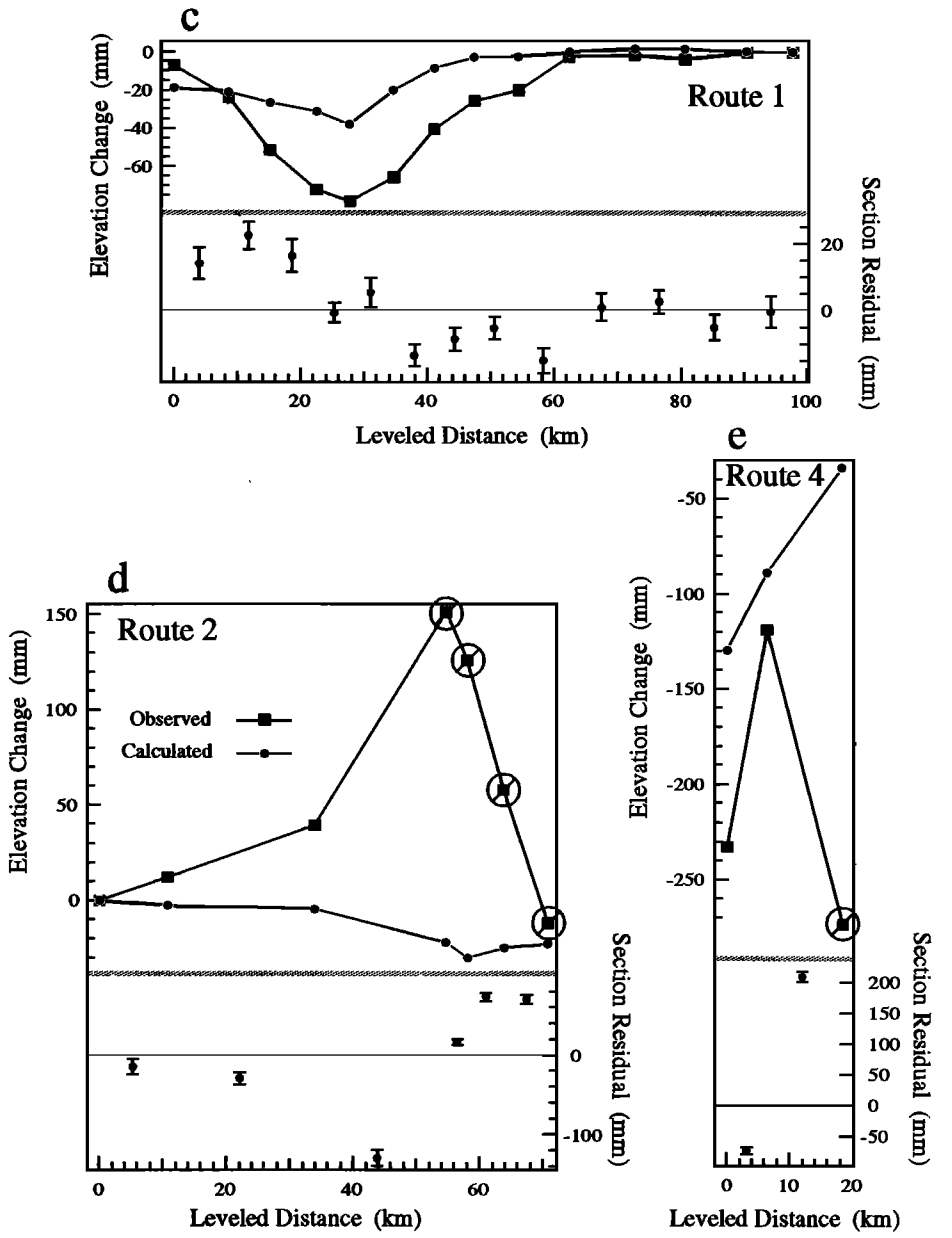

Figure 5. (continued)

techniques to quickly converge on the minima might be more efficient and reliable than using either technique by itself.

Confidence Regions

We assess the range in fault geometries that provide an adequate fit to the data by examining all models whose χ^2 is less than a particular value χ^2_α. We use pure random sampling over a uniform distribution of S to generate trial models. To approximate the confidence region, we use an F ratio test, which assumes that the observations are normally distributed and that the minimization function can be linearized in the vicinity of the global minimum. Given the χ^2 for the optimal model, χ^2_{opt}, all models with $\chi^2 < \chi^2_\alpha$ are consistent with the optimal model at the $100 \times \alpha\%$ confidence level, where

$$\chi^2_\alpha = \chi^2_{opt}\left[1+\frac{m}{n-m}F(m,n-m,1-\alpha)\right] \quad (4)$$

Table 5. Coastal Uplift Observations

Observation Site	Latitude, ° N	Longitude, ° W	Uplift, mm	Sigma, mm
Bear River Ridge	40 29 16	124 23 13	0	150
Cape Mendocino	40 26 10	124 24 26	670	100
Steam Boat Rock	40 24 55	124 23 45	900	150
Devils Gate	40 24 12	124 23 6	960	100
Mussel Rock	40 20 51	124 21 54	1470	220
Sea Lion Rock	40 19 29	124 20 59	990	180
Mattole Point	40 18 17	124 21 10	810	150
South Mattole Point	40 16 36	124 21 45	710	190
Fourmile Creek	40 15 22	124 21 24	380	60
Lighthouse	40 14 54	124 20 55	310	150
Sea Lion Gulch	40 14 23	124 19 50	0	150
Cooskie Creek	40 12 15	124 18 11	0	150

Table 6. Normalized RMS of Optimal Models

Data[a]	n	Model[b] A	Model[b] B	Model[b] C	Strike, Dip Fixed[c]	95% Limit[d]
A	139	4.59	10.17	12.87	5.73	5.01
B	125	3.06	2.48	2.59	2.75	2.73
C	51	3.84	2.54	2.40	2.47	3.05

[a]A, GPS, coastal uplift, all leveling; B, GPS, coastal uplift, route 1 leveling; C, GPS, coastal uplift.
[b]Optimal model parameters given in Table 7.
[c]Seismic moment tensor estimate of fault strike and dip assumed.
[d]Confidence limit of 95% (F ratio test).

and m is the number of model parameters, n is the number of data, and F is the F distribution with m and $n-m$ degrees of freedom [e.g., *Draper and Smith*, 1981]. In this case, the model parameters include the seven randomly varied parameters and the two explicitly estimated parameters (m = 9). The confidence region for each parameter is then determined from the range of values given by all the models consistent with the optimal model at the specified confidence level. A disadvantage of using the F ratio test to define a confidence region is that it makes assumptions regarding the distribution of errors and the shape of the minimization function near the global minimum. *Árnadóttir and Segall* [1994] found that the F ratio test tends to underestimate confidence regions slightly relative to those predicted by bootstrapping techniques that rely on random resampling of the original data [e.g., *Efron and Tibshirani*, 1986].

Results

Optimal Models

We determined optimal models using three subsets of the observations to test for self-consistency between the different measurement techniques. Data set *A* uses all the data (13 three-component GPS relative vectors, 12 coastal uplift observations, and 88 leveling section-elevation differences, n = 139), data set *B* includes only the GPS, coastal uplift and route 1 leveling data (n = 125), and data set *C* includes only the GPS and coastal uplift data (n = 51). Table 6 summarizes the misfit of the optimal models estimated using these subsets in terms of the normalized root mean squared (nrms) residual, equal to $(\chi^2/(n-m))^{1/2}$. The nrms residual, a physically intuitive measure of misfit, is the ratio of the average scatter in the data to their formal errors. Table 7 gives the estimated fault parameters for the optimal models. In all cases we used the formal errors to weight the data and assumed the observations to be uncorrelated. For each data set, we performed several random walks in the minimization function using different initial models and found that the random cost algorithm uniformly converged on the global minimum.

The optimal model for data set *A* ("model *A*"), which uses all the data, indicates that rupture was on a thrust fault shallowly dipping to the southeast. The optimal model has an nrms residual of 4.59 and resolves 4.9 m of slip on a rectangular fault 14 km in along-strike length and 15 km in downdip width (Figure 1). The strike of the fault is N22°E and it dips 28° SE. It extends from 1.5 to 8.7 km in depth. The rake of the slip vector is 135°, which implies 3.5 m of thrust dip-slip motion and 3.5 m of right-lateral strike-slip motion. Assuming the crust has a rigidity of 30 GPa, the estimated geodetic moment is 3.1×10^{19} N m, or moment magnitude M=7.0 [*Hanks and Kanamori*, 1979].

Oppenheimer et al. [1993] concluded that the fault ruptured on a shallow landward dipping plane primarily by comparing the seismic focal mechanism (Figure 1) with the distribution of aftershock locations. We tested whether the geodetic data alone included enough near-field observations to distinguish between the shallow and steeply dipping orthogonal nodal planes. To ensure rupture on a steeply dipping reverse fault, we allowed the random walk to sample only dips greater than 45° and azimuths between 90° and 270° We found a local minimum

Table 7. Fault Parameters for Optimal Models

Data[a]	Location[b] East, km	Location[b] North, km	Location[b] Depth, km	Strike,[c] °N	Dip,[c] °E	Rake,[c] deg	Slip,[c] m	Width,[d] km	Length,[d] km	Moment,[e] $\times 10^{19}$ N m
				Unconstrained Model						
A	$-11.8^{+2.3}_{-2.8}$	$3.7^{+2.6}_{-1.7}$	$5.1^{+2.3}_{-3.5}$	$21.8^{+17.2}_{-17.1}$	$28.1^{+20.2}_{-20.4}$	$135.4^{+19.0}_{-18.1}$	$4.9^{+18.2}_{-1.3}$	$15.2^{+8.3}_{-9.8}$	$13.7^{+3.0}_{-4.9}$	$3.1^{+2.4}_{-0.8}$
B	$-10.7^{+3.9}_{-4.9}$	$4.7^{+2.2}_{-2.3}$	$6.6^{+4.0}_{-2.7}$	$-6.5^{+26.1}_{-36.2}$	$26.9^{+10.8}_{-11.2}$	$98.3^{+27.6}_{-41.5}$	$3.6^{+34.8}_{-1.5}$	$18.8^{+17.1}_{-9.3}$	$15.6^{+9.3}_{-14.4}$	$3.2^{+1.3}_{-0.7}$
C	$-8.8^{+3.5}_{-5.6}$	$5.2^{+2.5}_{-2.2}$	$6.8^{+4.2}_{-2.5}$	$-7.6^{+41.5}_{-34.9}$	$20.3^{+15.6}_{-12.9}$	$96.9^{+45.7}_{-40.3}$	$3.0^{+36.1}_{-1.2}$	$16.8^{+22.2}_{-10.0}$	$18.9^{+9.1}_{-17.7}$	$2.9^{+1.2}_{-0.5}$
				Strike = –10.3°, Dip = 13.0° Constrained[f]						
A'	–10.3	2.5	2.7	–10.3	13.0	110.9	5.7	10.6	16.7	3.0
B'	–6.3	5.7	5.3	–10.3	13.0	89.3	4.1	9.5	21.8	2.6
C'	–6.9	5.7	7.1	-10.3	13.0	92.6	2.9	14.1	21.8	2.7

Uncertainties are 95% confidence range based on F ratio test comparison to optimal model.
[a]Data sets are A, GPS, coastal uplift, all leveling; B, GPS, coastal uplift, route 1 leveling; C, GPS, coastal uplift.
[b]Location is the center of the fault, with east and north relative to mainshock hypocenter.
[c]Strike, dip, rake, and slip in the convention of *Aki and Richards* [1980].
[d]Fault dimensions are downdip width and along-strike length.
[e]Assumes a rigidity of 30 GPa.
[f]Constraints from surface wave moment tensor analysis [*Oppenheimer et al.*, 1993].

associated with models having an nrms residual of 4.86 that have nearly vertical fault planes striking about 145°. Using the F ratio test (equation (4)), all models with an nrms residual ≤ 5.01 are consistent with the optimal model (nrms residual = 4.59), at the 95% confidence level (Table 6). The vertical fault plane models differ from the optimal model at the 82% confidence level and have several unrealistic characteristics, including a short along-strike length (3 km), a large slip magnitude (16 m), and a long downdip width (30 km) that extends to nearly triple the hypocenter depth (10.6 km). Other models whose fault dimensions were constrained to more realistic values have nrms residuals that are not consistent with the optimal model at the 95% confidence level. Therefore we believe the geodetic observations to a high degree of confidence can distinguish between the orthogonal nodal planes and favor rupture on a shallowly dipping thrust fault.

Model Misfit

The model *A* has a normalized rms residual of 4.59, significantly greater than 1. An nrms residual near 1 implies that the formal errors are consistent with the observed scatter, whereas an nrms residual significantly greater than 1 can mean that the formal errors are underestimated, that data outliers or blunders are present, that the data are systematically biased, or that the assumed physical model is inadequate.

The formal errors of GPS and leveling surveys are well understood from previous studies [e.g., *Bomford*, 1980; *Davis et al.*, 1989; *Marshall and Stein*, 1996] and are probably not greatly underestimated. The uncertainties of the coastal uplift observations are less well understood. However, the nrms residual of the optimal model using only the coastal uplift observations is 0.98, suggesting that the uncertainties we assigned to them are consistent with their scatter and that the residuals of the tidal uplift observations do not contribute much to the misfit (Figure 5a).

The nrms residual of the model *A* including only GPS observations is 4.51. The most significant discrepancies are in the north components at stations Rohnerville, Bear Rdg 2, and King Peak 2 (8–10σ outliers) (Figure 3). We have no compelling reason to reject these or any other GPS observations, because they were collected using the same equipment, processed in a uniform manner, and span a short time interval that can be corrected for interseismic deformation. The most suspect GPS displacement is Pierce Ecc, which may include a small coseismic contribution due to the Honeydew earthquake. We estimated an optimal model using all the data except Pierce Ecc. This model had a nrms residual of 4.64 and fault parameters essentially the same as model *A*.

The observations most misfit by the model *A* are the leveling data, which have an nrms residual of 5.18. Several leveling observations may be outliers or blunders. The residual with the largest contribution to the total χ^2 (a 36σ outlier) corresponds to the leveling section-elevation difference between BMs LV0362 and LV0363 (Figure 5b). The nrms residual of model *A* including all the data except this section-elevation difference is 3.35, a significant improvement. Removing additional observations also improves the nrms residual, although less significantly. However, we do not have a simple reason to reject these leveling observations, unlike other observations we believe may have been affected by the 1991 Honeydew earthquake or by subsidence due to groundwater withdrawal (see Appendix).

The leveling observations along route 1 (Figure 5c), which were measured with modern instruments and span a short coseismic interval that can be corrected for interseismic deformation (see Appendix), are well understood. The leveling observations on routes 2, 3, and 4, which are closer to the epicentral region and thus contribute more information to the model estimate, are more problematic. Before 1992, these routes were surveyed only in 1935 except for a part of route 3, which was resurveyed in 1942 to correct problem with the 1935 survey that could not be resolved by NGS. Analysis on these routes of double-run sections and circuit misclosure corrected for interseismic deformation along route 1 indicate that the data are self-consistent with precision exceeding second-order leveling specifications. However, relatively few BMs from these surveys were recovered in 1992 postearthquake survey, making assessment of systematic errors associated with miscalibrated leveling rods particularly weak. The error analysis is also insensitive to interseismic deformation that may have occurred near the coast during the 57-year interval between surveys.

Data Subsets

To test whether the leveling data are systematically biased, we estimated several models using subsets of the leveling data. Because many of the BMs for routes 2, 3, and 4 became lost or damaged in the 57-year interval between 1935 and 1992, the average BM spacing along those routes is 9 km, whereas route 1 has a spacing of 1 km. Thus the data along route 1, which have little signal compared to the other routes, would have 3 times greater influence on the inversion than the rest of the leveling data, owing to missing BMs and not to a difference in survey precision. *Marshall* [1992], in a study of Loma Prieta leveling data, found that the optimal models using all the data were biased toward a line source with little downdip extent, indicating the dependence on far-field data, but that decimation of the high-density data reduced this bias and produced model faults consistent with the distribution of aftershocks. We tested for this bias by decimating the route 1 BMs to have an average 9 km spacing (large leveling symbols in Figure 4). The optimal model using the decimated leveling data was essentially identical to model *A*, suggesting that the high signal-to-noise ratio of the leveling data, especially along route 3, dominates the inversion for model *A*. This may also explain why the route 1 data are systematically misfit by model *A* (Figure 5c).

Therefore we estimated optimal models using data that excludes the high signal-to-noise leveling data. The optimal model for data set *B* ("model *B*"), which excludes leveling data from routes 2, 3, and 4, has an nrms residual of 2.48 (Table 6), significantly better than model *A*. The horizontal displacement at the station Bear Rdg 2, which was significantly misfit by model *A*, is predicted well by model *B* (Figure 3). Many of the fault parameters, such as the dip, location, and fault dimensions for model *B* are similar to model *A* (Table 7). The most significant differences are the estimated strike of the fault plane and rake of the slip vector. The strike of the fault for model *B* is –6.5°N and the rake is 98.3°, both of which are more consistent with the seismic moment tensor inversion (Figure 1). It resolves 3.6 m of slip on a slightly larger fault plane than model *A*, so that the estimated geodetic moment of 3.1×10^{19} N m is nearly equal to the model *A* estimate.

The optimal model for data set *C* ("model *C*"), which excludes all the leveling data, has an nrms residual of 2.40, slightly better than model *B* (Table 6). Model *C* has a shallower dip of 20° NE than model *A* or *B*. It resolves 3.0 m of slip on a plane similar to model *B*, so the estimated geodetic moment of 2.9×10^{19} N m is less than model *A* or *B*. Model *C* is very similar, except for having a slightly steeper dip, to the results of our previous analysis based on the same GPS observations and preliminary coastal uplift observations [*Oppenheimer et al.*, 1993].

Model Uncertainty

To assess the uncertainties of these models, we compared the nrms residual resulting from trial fault geometries, made by randomly varying the seven parameters describing the fault geometry and estimating the slip vector, with the nrms residual of the optimal using the F ratio test (equation (4)). All models with an nrms residual less than the 95% limit listed for each model in Table 6 are consistent with the optimal model at the 95% confidence level. Using data set *A*, for example, we found 2000 models with nrms residual less than 5.01 that are consistent with model *A* at the 95% confidence limit. The range of each parameter value at the 95% confidence level for models *A*, *B*, and *C*, each estimated from about 2000 trial models, is given in Table 7. The location of the center of the fault for each model is resolved to within about 4 km. The strike and dip of the fault for each model is poorly resolved (about ±20°). The models resolve at least 2 m of slip on the fault, but as much as 40 m is permissible. These high values usually correspond to faults with unrealistically small fault dimensions. The inverse correlation between slip and width or length is demonstrated when they are multiplied together to give a stable estimate of the geodetic moment, which have a range of $2.3–5.5\times10^{19}$ N m ($6.9 \leq M \leq 7.1$). Although the range of model *A* for geodetic moment is consistent with the seismic moment of 4.45×10^{19} N m (M=7.1) estimated from surface-wave moment tensor inversion [*Oppenheimer et al.*, 1993], the optimal value of 3.1×10^{19} N m is about 70% of the seismic estimate.

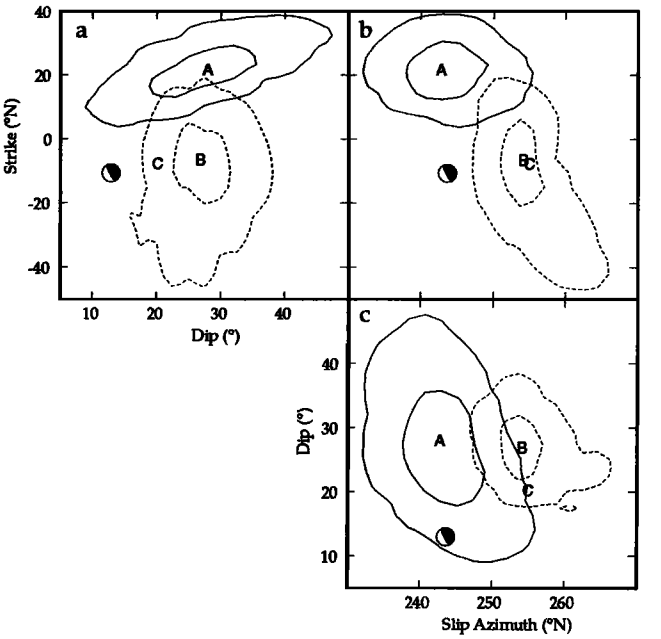

Figure 7. Monte Carlo estimates of the focal mechanism parameters of the fault. (a) Dip versus strike, (b) slip azimuth versus strike, (c) slip azimuth versus dip. Slip azimuth is the azimuth of the slip vector that has been projected to the surface. See Figure 6 for description of confidence regions. Focal mechanism, location of strike, dip, and rake of the surface wave moment tensor estimate [*Oppenheimer et al.*, 1993].

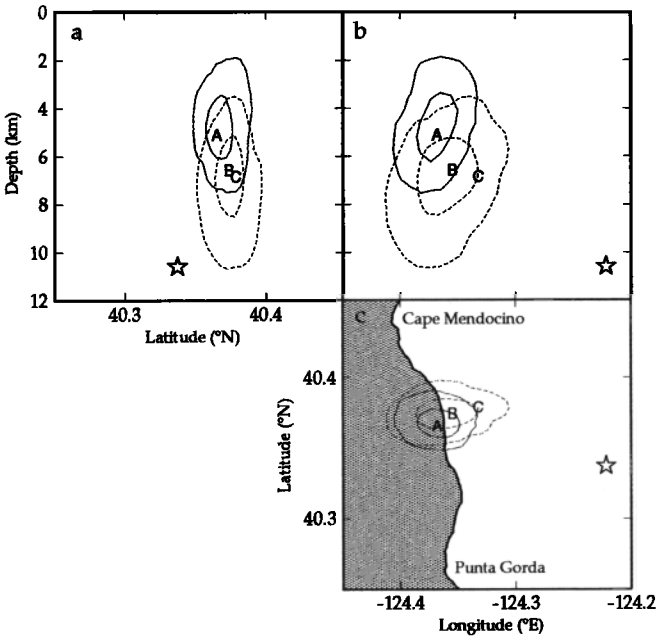

Figure 6. Monte Carlo estimates of the location of the center of the fault. (a) Latitude versus depth, (b) longitude versus depth, and (c) longitude versus latitude. Letters indicate the position of the optimal fault models *A*, *B*, and *C*. Inner and outer contours show the 50% and 95% confidence regions for the parameters, respectively. Solid contours are for model *A*, dashed contours are for model *B*. Contours for model *C* are similar to model *B*, and have been omitted for clarity. Star, 1992 M=7 Cape Mendocino mainshock.

We determined the confidence level for each trial model compared to its optimal model and contoured these values to show some of the trade-offs between parameters in Figures 6–8. In each figure we show the optimal model location, denoted by the model letter, and contour the 50% and 95% confidence levels for models *A* and *B*; for clarity sake, we do not show the confidence levels for model *C* , which are similar to model *B*. The trade-off between the center of the fault location parameters (latitude, longitude, and depth), compared to the mainshock hypocenter is shown in Figure 6. All models give a similar location for the center of the slip patch, northwest, and above the hypocenter.

The trade-off between the parameters describing the focal mechanism (strike ϕ, dip δ, and rake λ) compared to the surface-wave moment tensor are shown in Figure 7. The strike of model *A* is significantly different than models *B* and *C*, and the seismic estimate of −10.3°N. All the models in general predict a steeper dip than the seismic estimate of 13.0°, although some of the trial models for data set *A* do have dips less than 13°. The strike and rake are highly correlated for faults with shallow dips because the rake must change as the strike of the fault varies to maintain a consistent displacement of crustal material. Because of this strong correlation, we plot

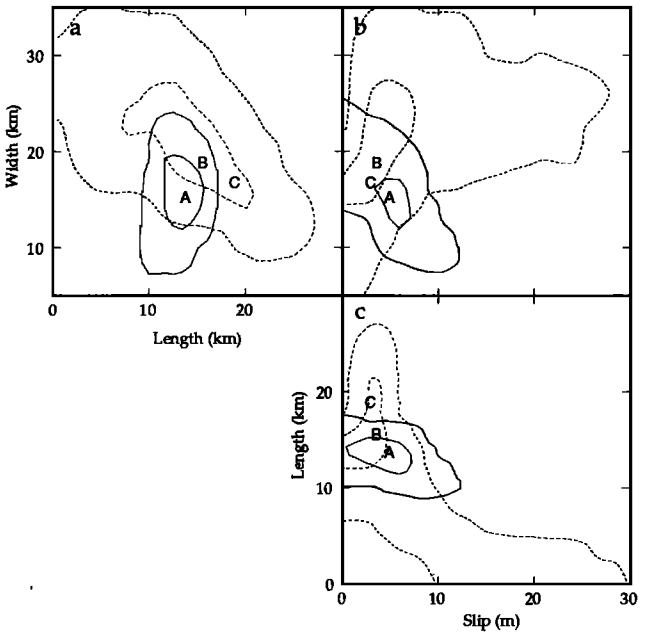

Figure 8. Monte Carlo estimates of the fault dimensions and slip. (a) Length versus width, (b) slip versus width, (c) slip versus length. See Figure 6 for description of confidence regions.

the slip azimuth $\theta = \phi - \tan^{-1}(\tan\lambda \cos\delta)$, which is the azimuth with respect to north of the slip vector projected to the surface. The slip azimuth of model *A* agrees well with the seismic moment tensor estimate (243.7°).

The trade-off between the width, length, and slip parameters are shown in Figure 8. The dimensions of the fault, particularly its along-strike length, are much better resolved by model *A*. This is probably due to the leveling data along routes 2, 3, and 4 that are directly above the fault and therefore provide strong constraints on its dimension. High-slip values for model *B* correspond to very short along-strike fault lengths. On the other hand, for model *A*, because the fault length is well resolved, high-slip values correspond to narrow fault widths (we found slip up to 23 m is permissible, although these high values are not evident due to limitations in how we contoured the observations).

Model Consistency

The optimal fault dip inferred from models *A*, *B*, and *C* are all greater than the 13.0° determined by surface-wave moment tensor analysis [*Oppenheimer et al.*, 1993] (Figure 7). To test how consistent the geodetic data are with the seismic moment tensor, we estimated optimal fault models using data sets *A*, *B*, and *C*, while constraining the dip and strike at the seismically determined values. The nrms residuals for these models are given in Table 6 and the fault parameters are given in Table 7. Although the constrained model inferred using data set *A* has the closest rake of the three models to the seismic estimate (105.6°), it has an nrms residual of 5.73, and is therefore not consistent with the unconstrained model *A* (Table 6). The constrained model using data set *B* is consistent with its unconstrained model at about the 95% confidence level. The constrained model using data set *C*, which is nearly identical to the dislocation model given by *Oppenheimer et al.* [1993], is not statistically different than the unconstrained model *C*. These results suggest that the leveling data are not consistent with the seismic moment tensor estimate.

We use the F ratio test (equation (4)) to check the consistency between models *A*, *B*, and *C*, and show the results in Table 6. If we assume the fault parameters are given by model *A*, the nrms residual using the data set *B* is 3.06 and the nrms residual using data set *C* is 3.84. Both of these nrms residuals are greater than the 95% confidence level limit of the optimal models *B* and *C* (2.73 and 3.05, respectively), therefore model *A* is not consistent with either model *B* or *C*. Similar analysis on models *B* and *C* indicate that they are not statistically different at the 95% confidence level, but they are different than model *A* (Table 6).

These results suggest that the older leveling observations in the epicentral region may be inconsistent with the other data. Because none of the BMs along routes 2, 3, and 4 were measured before and after the earthquake with both GPS and leveling, we cannot directly evaluate the problem. One possible explanation is unmodeled interseismic deformation. However, the only direct measurement of interseismic deformation near the coast are the Geodolite trilateration observations of horizontal deformation made during the interval 1981–1989, and our preliminary efforts to model these observations are not yet adequate to estimate the vertical interseismic deformation. The meter-level uplift observed at the two coastal leveling BMs, LV0368 and LV0369, is fit reasonably well by the model *A* predictions, and is consistent with the nearby coastal uplift observations within their 2σ uncertainty (Figure 6a). If this comparison is valid, the agreement between the leveling and coastal uplift places weak limits, at the 20 to 30-cm level, on the amount of interseismic deformation that may have affected the older level observations. However, detailed geologic and geomorphic studies indicate that the two leveling benchmarks are located in an area that has shattered bedrock and the greatest density of landslides in the region (D. Merritts, personal communication, 1995). Although the benchmarks show no obvious signs of disturbance, it is possible that deep-seated landslides have moved a large area around them.

Thus we are faced with a dilemma. On the one hand, we have evidence that the leveling data along routes 2, 3, and 4 are inconsistent with the other data, possibly due to unmodeled interseismic deformation or to nontectonic disturbance of the benchmarks. On the other hand, if these data are valid, they could provide critical information for resolving greater details about the geometry and slip on the fault. It is likely that future modeling work using a more realistic fault model that allows the slip to vary from place to place on the fault may resolve the apparent inconsistencies in the data. Given the uncertainties in our present models, we will emphasize the most robust results derived from common features of all three optimal models in the following discussion.

Discussion

Earthquake Slip and Plate Convergence

Based on the optimal models, the geodetic slip azimuth of the Cape Mendocino earthquake is well resolved and is approximately 250±10°N, in agreement with the seismic slip estimate (Figure 7). The geodetic slip azimuth is also consistent with the convergence of North America with respect to the Juan de Fuca plate. Figure 1 shows the relative

velocities of the Pacific, North America, and Juan de Fuca plates at the approximate position of the Mendocino triple junction (N40°20', W124°20'). The NUVEL-1A global plate motion model, which includes recent revisions to the geomagnetic timescale [*DeMets et al.*, 1990; *DeMets et al.*, 1994], predicts 44.7 mm/yr at N27.5°W for the relative motion of the Pacific plate with respect to North America. Convergence across the Cascadia megathrust at the triple junction is more difficult to estimate because the southernmost Juan de Fuca plate is deforming internally. The relative motion of the Gorda deformation zone with respect to North America is not well known. For simplicity, we assume that *Wilson*'s [1993] estimate of the relative motion of the Juan de Fuca plate with respect to the Pacific plate for the NUVEL-1 averaging interval (3.075 m.y.) is approximately correct. Given these assumptions, the relative horizontal motion of North America with respect to the Juan de Fuca plate is 34.7 mm/yr at 240.6°N at the triple junction (Figure 1). The convergence direction differs by only 10° from the estimated geodetic slip azimuth of 250±10°N.

Relation to Aftershocks

The location of the optimal model faults match the shallow aftershock seismicity and are closely aligned with the south end of the Cascadia megathrust deformation front. The fault locations for models *A* and *B* with respect to the aftershocks that occurred within 5 days of the mainshock are shown in Figure 9. The fault geometry for model *C* is similar to model *B*; the following relationships refer to the model *A* fault but are common to all three fault models. The bottom edge of the plane lies within 4 km of the hypocenter and the plane project to hypocenter. This suggests that rupture initiated at depth and propagated updip to the northwest, and that most of the slip was accommodated at shallow depths. This slip pattern is similar to that observed in the 1994 Northridge earthquake, which occurred on a buried thrust fault [*Hudnut et al.*, 1994]. The top of the fault plane lies at shallow depths offshore, consistent with the absence of observed surface faulting onshore. The fault lies just north of an east-westward trend of seismicity extending to a depth of 25 km that may define the position of the Mendocino transform fault [*Oppenheimer et al.*, 1993] and overlies most of the shallow aftershock seismicity (<12 km deep), including a north-northwestward trend beneath Cape Mendocino close to the north limit of the rupture zone. The south edge of the geodetic fault is nearly aligned with the southernmost edge of the deformation front of the Cascadia subduction zone at the base of the continental slope (Figure 1), which is mapped to within 15 km of the coast before it becomes indistinct [*Clarke*, 1992].

The geodetic observations image a fault that appears to be located at or several kilometers above the shallow aftershock zone (Figure 9). We do not believe there is a significant discrepancy between the imaged fault and the aftershock locations for two reasons. First, the optimal depth to the center of the fault (5–7 km) has a 1.6–11 km range of uncertainty at the 95% confidence level (Table 7), which encompasses the entire shallow aftershock zone. In addition, we assumed a homogeneous half-space model, which can underestimate the depth of the fault if the crust is composed of a compliant layer over a stiffer half-space [e.g., *Árnadóttir et al.*, 1991; *Stein and Ekström*, 1992; *Marshall and Stein*, 1996]. For example, *Stein and Ekström* [1992] used a two-dimensional boundary-element model with a rigidity contrast factor of 3.5 to show that the compliant upper layer tended to concentrate surface deformation and that the fault depth had been underestimated by 1.5 km. The crustal structure near the Mendocino triple junction is likely to be very heterogeneous, where the material above the thrust fault is probably in the subduction zone forearc and has a lower rigidity than the material in the subducting plate below.

Owing to uncertainties in the geodetic fault location, both from noise in the data used to estimate the fault location and from possible inhomogeneities in the medium, we cannot discriminate between interplate rupture on the megathrust and intraplate rupture in the forearc above. However, both the orientation of the slip parallel to plate convergence and the location of the shallowly dipping thrust fault in alignment with the subduction zone deformation front suggest that the

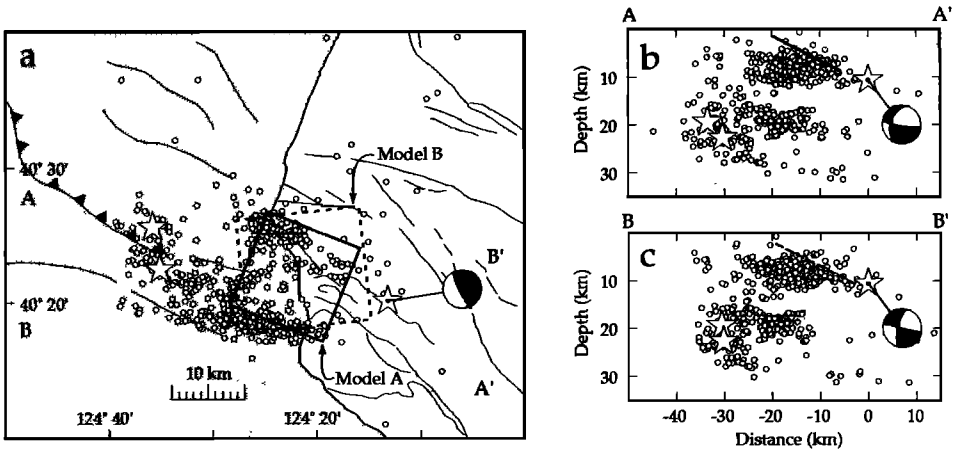

Figure 9. Seismicity for 5-day interval after April 25, 1992, Cape Mendocino earthquake. Stars, mainshock and two large aftershocks located offshore; circles, smaller aftershocks. (a) Solid rectangle, surface projection of optimal model *A* using all data; dashed rectangle, optimal model *B* excluding leveling data along routes 2, 3, and 4. (b) Vertical cross section A-A', normal to strike of model *A* fault plane. (c) Vertical cross section B-B', normal to strike of model *B* fault plane. The mainshock focal mechanism is projected to the vertical plane of each cross section.

mainshock relieved strain associated with the southernmost segment of the Cascadia megathrust.

Earthquake Recurrence

If the mainshock accommodated slip on the Cascadia megathrust, a comparison of the slip vector with the predicted relative plate motions provides a constraint on the expected recurrence interval for such events. Assuming that the 1992 M=7 Cape Mendocino earthquake is characteristic for the southernmost segment of the Cascadia subduction zone and that relative plate motion is entirely accommodated by repetition of such events, the recurrence interval can be estimated by dividing the horizontal-slip magnitude of 4.9 m, with a range of 3.6–23.1 m (model *A*, Table 7), by the plate convergence rate of 34.7 mm/yr derived from studies of Juan de Fuca–North America relative plate motion. The predicted recurrence interval for this characteristic earthquake is 140 years, with a range of 100–670 years. The recurrence interval predicted by the other models ranges from 60 to 1100 years, with the longest intervals corresponding to unrealistically large values of slip. If we assume the along-strike length of the fault is 10–20 km, which includes most of the acceptable models, the estimated slip ranges between 2 and 10 m (Figure 8), and the recurrence interval is 60 and 280 years.

The coseismic uplift is located in an area of high Quaternary uplift (Figure 10), estimated to be rising at >1 mm/yr over the past 120,000 years from studies of marine and inland fluvial deposits [*McLaughlin et al.*, 1993]. The coseismic subsidence lies largely to the north of the area of Quaternary uplift. These observations suggests that Quaternary uplift near Cape Mendocino may result from repeated coseismic uplift, in events similar to the 1992 M=7 Cape Mendocino earthquake, that is not entirely canceled by interseismic deformation [e.g.,

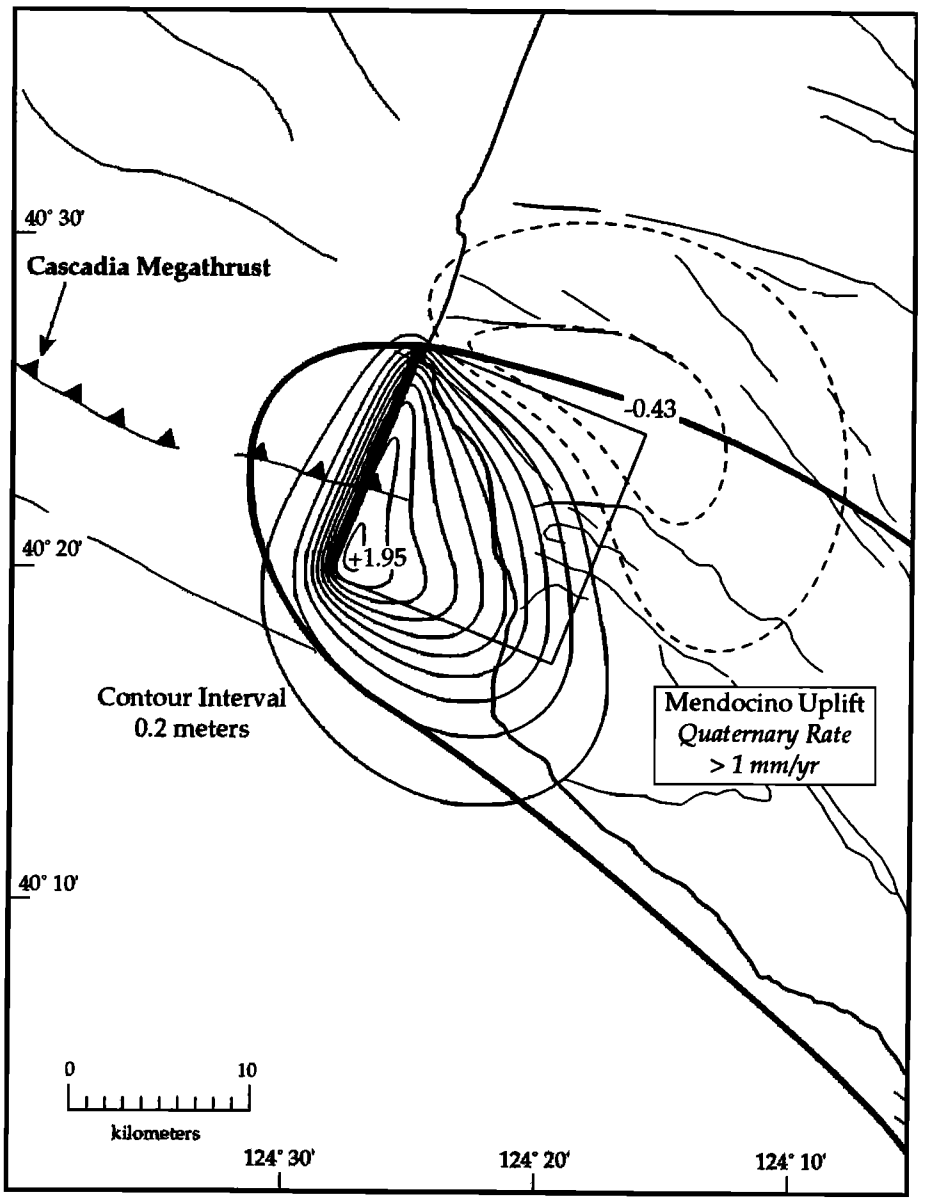

Figure 10. Coseismic uplift and subsidence predicted by optimal fault model (rectangle) compared to region of high Quaternary uplift rates. Coseismic uplift contoured in 0.2-m intervals, solid for uplift and dashed for subsidence. Bold line bounds region of high Quaternary uplift rates, estimated to be greater than 1 mm/yr from marine terrace and inland fluvial deposit studies [*McLaughlin et al.*, 1993].

King et al., 1988; *Stein et al.*, 1988]. Theoretical studies are divided as to whether cycles of earthquake on subduction zone interfaces result in permanent deformation. *Matsu'ura and Sato* [1989] presents a model that yields long-term uplift rates compatible with the formation of marine terraces. On the other hand, *Savage* [1983] presents a model suggesting that interseismic deformation tends to cancel coseismic deformation due to earthquakes on the plate interface, yielding no long-term vertical deformation. If this model is correct, one possible mechanism for long-term uplift is rupture on imbricate faults in the overlying forearc that do not accommodate the long-term plate convergence.

Several studies have inferred uplift rates from Quaternary marine terraces found along the coast from Cape Mendocino to Point Delgado. *Merritts and Bull* [1989] inferred an uplift rate of 3–4 mm/yr from Pleistocene terraces. *Lajoie et al.* [1982] inferred a similar rate from a few Holocene terraces near Cape Mendocino. A recent study of more than 20 Holocene terraces between Cape Mendocino and Point Delgada suggests an average 2–3 mm/yr uplift, although the rates appear to be highly variable along this part of the coast, with the deformation from Punta Gorda to Point Delgada having a different rate, timing, and pattern of uplift than area of 1992 coseismic uplift (D. Merritts, personal communication, 1995). If the Holocene uplift is due entirely to deformation caused by repeated characteristic earthquakes followed by no interseismic relaxation, then the recurrence interval would be equal to the predicted coseismic uplift, which is about 0.8 m averaged along the coast (Figure 5a), divided by the Holocene uplift rate of about 2–4 mm/yr, or 200–400 years. Interseismic relaxation would decrease this recurrence interval. Of course, less frequent M=8+ megathrust events may also occasionally rupture this southernmost portion of the Cascadia subduction zone and cause much greater coseismic deformation; the recent study of the Holocene terraces finds evidence for uplift of ~3.5–4.5 m recurring at least every 1300 years (D. Merritts, personal communication, 1995). The actual history of uplift in this region is likely to be due to a combination of M7 and M8+ events.

Conclusions

The slip associated with the 1992 Cape Mendocino earthquake occurred on a shallowly dipping thrust fault in a direction nearly parallel to the convergence between the North America and Juan de Fuca plates. The event relieved strain associated with the southernmost segment of the Cascadia subduction zone and occurred on the megathrust or immediately above in the forearc. The earthquake uplifted about 25 km of the coast south of Cape Mendocino that previously had been recognized for its high rates of Holocene and Pleistocene uplift. We infer that this segment of the Cascadia subduction zone has ruptured repeatedly in the past and that coseismic deformation may be a significant component of the long-term observed uplift patterns. If the 1992 M=7 Cape Mendocino earthquake is characteristic for this segment, its recurrence interval is about 100–300 years.

Although awareness of the seismogenic potential of the Cascadia subduction zone has increased significantly during the 1980s [e.g., *Heaton and Kanamori*, 1984; *Heaton and Hartzell*, 1987; *Atwater*, 1987; *Clarke and Carver*, 1992], the 1992 Cape Mendocino earthquake is the first well-recorded event to demonstrate that potential. The earthquake struck at shallow depth in a region cut by numerous active surface faults, but none of these faults slipped during the event. In common with several other damaging earthquakes that have occurred in California since 1980, such as the 1983 M=6.5 Coalinga, 1985 M=6 Kettleman Hills, 1987 M=6 Whittier Narrows, 1992 M=6 Sierra Madre, and 1994 M=6.7 Northridge earthquakes, the fault was blind. These earthquakes occurred in areas undergoing crustal shortening beneath geologically young folds or, in the case of Cape Mendocino, beneath rapidly uplifting marine terraces. As such, the 1992 Cape Mendocino earthquake emphasizes the need for detailed seismic, geomorphic, and geodetic studies of areas of active folding and uplift whose seismogenic potential may be currently underestimated or unrecognized.

Appendix: Leveling Corrections

To isolate the coseismic signal, we made a correction to the heights observed in 1992 along route 1 (Figure 4). The correction is based on observed elevation-change rates during the interseismic interval 1967–1988; the 1931 survey had too few benchmarks in common with the 1967 and 1988 surveys to make a comparison possible. The corrected and uncorrected coseismic elevation changes, the elevation change rates for 1967–1988, and the topography along route 1 are shown in Figure A1. The datum for the elevation change rate function was chosen by averaging the near-zero rates of BMs with bedrock settings. The correction smooths the coseismic elevation changes, removing short-wavelength components unrelated to tectonic deformation. A long-wavelength signal appears at the north end of the elevation change rate data (0-35 km) where the BMs, sitting on Quaternary alluvium in the Eel River basin (Figure 4), are subsiding at a rate of as much as 3.2 mm/yr. This long-wavelength signal could be due either to long-term compaction and expansion of the water-saturated alluvium or to interseismic tectonic motions, or to both. Because we have not examined water table records in this area and no definitive model of interseismic vertical motions exists, we can not determine the source of this deformation. For our analysis we assume that elevation changes measured by leveling during the interval 1967–1988 reflect ongoing deformation taking place between 1935 and 1992. The uncertainty associated with this assumption is reflected by our arbitrary assignment of 50% confidence in the subsidence corrections (equation (1)).

Random leveling errors were assessed in two ways. First, the agreement between forward and backward measurements of the height between BMs where sections were double run, $\alpha_{F\text{-}B}$, was computed for each survey (Table 3). Then, the misclosure or disagreement in height measured around each leveling circuit (Figure 4), was calculated to find α_{miscl} (Table A1). In the absence of systematic errors, the two estimates of α should be equal, which we generally found to be true, except on circuits that include the 1935 survey L6711/1 (circuits A, B, B+C). This route was releveled in 1942 (L9851) and NGS documents indicate that the new heights supersede the 1935 values, implying that there was an error in the earlier survey although no specific reasons were given. No sections were double-run on L6711/1 and several large outliers (spikes) appeared when heights were differenced to both the 1942 and 1992 surveys. Substituting L9851 (1942) for L6711/1 (1935) reduces the circuit A misclosure from 6.6 to 2.8, but slightly increases the misclosure of circuits B and (B+C). Noting that all preseismic circuits are closed with surveys that are not coincident in time and that misclosures tend to increase as the

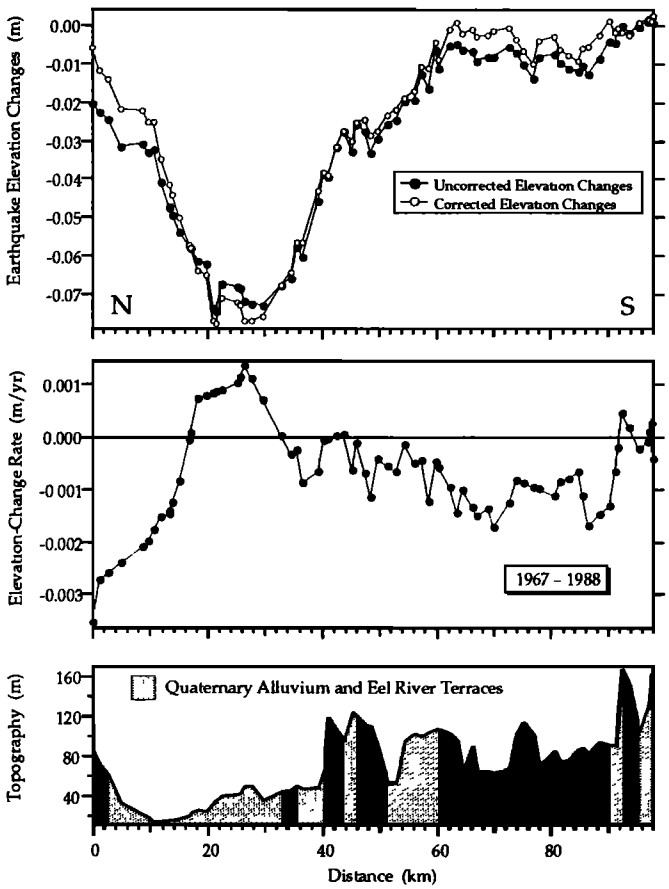

Figure A1. Profiles of leveling along highway 101. (Top) Observed uncorrected and subsidence-corrected elevation changes for earthquake interval 1988–1992. (Middle) Subsidence rate for interseismic interval 1967–1988 used for correction. (Bottom) Topographic profile with light gray areas showing the location of the Eel River basin and terraces, composed of Quaternary alluvium deposits.

time gap between surveys increases, we corrected the misclosure calculations by accounting for deformation during the missing time intervals. This correction employs the rates of elevation change measured during the interval 1967–1988, and assumes that those rates were constant during the interval 1935–1992. The correction reduced all misclosures to values comparable with the double-run $\alpha_{F\text{-}B}$, and all circuits that substitute the 1942 survey (L9851) for 1935 (L6711/1) have smaller misclosures after correction (Table A1). We therefore used the heights from the 1942 survey (where they were available) to construct coseismic elevation changes.

To assign uncertainty estimates to the leveling surveys we used a combination of the $\alpha_{F\text{-}B}$ and α_{miscl} values. For circuits A, B, C, A+B+C, postseismic leveling has an average $\alpha_{F\text{-}B}$, weighted by the number of double-run sections, of 1.07 and a weighted average α_{miscl}, weighted by the length of the circuits, of 0.85; we assigned $\alpha_{1992} = 0.96$, the average of those values. For preseismic leveling along route 1, corrected circuit misclosure (B+C[c]) is better than expected, so we assigned the more conservative estimate of $\alpha_{F\text{-}B} = 0.80$ to the 1988 survey. For preseismic leveling from 1935 and 1942 along routes 2 and 3, we assigned $\alpha = 1.90$, the average of the weighted average of α_{miscl} (corrected circuits A[a], B[a], C, A+B+C) and the weighted average of $\alpha_{F\text{-}B}$ for those surveys.

Table A1. Circuit Misclosures

Circuit	Dates	Circuit Length, km	Uncorrected Misclosure, mm	Uncorrected α_{miscl}, mm/√km	Corrected Misclosure, mm	Corrected α_{miscl}, mm/√km
		Preseismic Data				
A	1931,1935	68.8	+54.9	6.6	+63.3	7.6
B	1931,1935	162.6	–31.0	2.4	–37.4	2.9
C	1931,1935	131.1	–3.5	0.3	–3.5	0.3
A+B	1931,1935	177.4	+26.8	2.0	+25.9	1.9
B+C	1931,1935	209.7	–34.6	2.4	–40.9	2.8
A+B+C	1931,1935	224.6	+23.3	1.5	+23.3	1.5
A[a]	1931,1935,1942	68.8	–23.5	2.8	–8.7	1.1
B[a]	1931,1935,1942	162.7	+50.2	3.9	+34.6	2.7
(B+C)[a]	1931,1935,1942	207.5	+47.2	3.3	+31.5	2.2
(B+C)[b]	1935,1942,1967	203.6	–46.6	3.3	–5.8	0.4
(B+C)[c]	1935,1942,1988	204.3	–79.5	5.6	–5.7	0.4
		Postseismic Data				
A	1992	71.1	+14.4	1.7		
B	1992	152.0	–3.0	0.3		
C	1992	135.6	+6.5	0.6		
A+B	1992	162.4	+10.9	0.9		
B+C	1992	209.4	+2.7	0.2		
A+B+C	1992	228.1	+17.2	1.1		

All circuit misclosures are computed in a clockwise direction.
[a]Substitute L9851 (1942) for L6711/1 (1935).
[b]Substitute L21206 (1967) for L389 (1931).
[c]Substitute L25053 (1988) for L389 (1931).

The uncertainty for each coseismic datum is then calculated by combining these alpha values in (1).

Five BMs were removed because they showed elevation changes that differed markedly from computed deformation models of the Cape Mendocino earthquake (Table 4). Four BMs along route 2 lie close to the epicenter of the 1991 M=6.2 Honeydew earthquake and probably record surface deformation or disturbance from that event (Figure 5d). One BM along route 4 lies within the Eel River alluvium and probably is displaced by uncorrected subsidence effects (Figure 5e). Additional details regarding the processing of the leveling observations is given by *Stein et al.* [1993].

Acknowledgments. We thank Paul Bodin, Roland Bürgmann, Dorothy Merritts, Carl Mortensen, James Savage, and Paul Segall for thoughtful reviews. We thank Gary Carver, Angela Jayko, and David Valentine for providing coastal uplift results. The National Geodetic Survey provided leveling data collected with support from the Humboldt County Public Works department and the Federal Emergency Management Agency.

References

Aki, K., and P. G. Richards, *Quantitative Seismology: Theory and Methods*, 932 pp., W. H. Freeman, New York, 1980.

Arnadóttir, T., and P. Segall, The 1989 Loma Prieta earthquake imaged from inversion of geodetic data, *J. Geophys. Res.*, *99*, 21,835–21,855, 1994.

Arnadóttir, T., P. Segall, and P. Delaney, A fault model for the 1989 Kilauea South Flank earthquake from leveling and seismic data, *Geophys. Res. Lett.*, *18*, 2217–2220, 1991.

Arnadóttir, T., P. Segall, and M. Matthews, Resolving the discrepancy between geodetic and seismic fault models for the 1989 Loma Prieta, California, earthquake, *Bull. Seismol. Soc. Am.*, *82*, 2248–2255, 1992.

Atwater, B. F., Evidence for great Holocene earthquakes along the outer coast of Washington State, *Science*, *236*, 942–944, 1987.

Berg, B. A., Locating global minima in optimization problems by a random-cost approach, *Nature*, *361*, 708–710, 1993.

Bomford, G., *Geodesy*, 4th ed., 855 pp., Clarendon, Oxford, 1980.
Carver, G. A., A. S. Jayko, D. W. Valentine, and W. H. Li, Coastal uplift associated with the 1992 Cape Mendocino earthquakes, northern California, *Geology*, *22*, 195–198, 1994.
Clarke, S. H., Jr., Geology of the Eel River basin and adjacent regions: Implications for late Cenozoic tectonics of the southern Cascadia subduction zone and Mendocino triple junction, *AAPG Bull.*, *76*, 199–224, 1992.
Clarke, S. H., Jr., and G. A. Carver, Late Holocene tectonics and paleoseismicity, southern Cascadia subduction zone, *Science*, *255*, 188–192, 1992.
Cvijovic, D., and J. Klinowski, Taboo search: An approach to the multiple minima problem, *Science*, *267*, 664–666, 1995.
Davis, J. L., W. H. Prescott, J. L. Svarc, and K. J. Wendt, Assessment of Global Positioning System measurements for studies of crustal deformation, *J. Geophys. Res.*, *94*, 13,635–13,650, 1989.
DeMets, C., R. G. Gordon, D. F. Argus, and S. Stein, Current plate motions, *Geophys. J. Int.*, *101*, 425–478, 1990.
DeMets, C., R. G. Gordon, D. F. Argus, and S. Stein, Effects of recent revisions to the geomagnetic reversal time scale on estimates of current plate motions, *Geophys. Res. Lett.*, *21*, 2191–2194, 1994.
Dengler, L., G. Carver, and R. McPherson, Sources of North Coast seismicity, *Calif. Geol.*, *45*, 40–53, 1992.
Draper, N. R., and H. Smith, *Applied Regression Analysis*, 2nd ed., 709 pp., John Wiley, New York, 1981.
Efron, B., and R. Tibshirani, Bootstrap methods for standard errors, confidence intervals, and other measures of statistical accuracy, *Stat. Sci.*, *1*, 54–77, 1986.
Ekström, G., R. S. Stein, J. P. Eaton, and D. Eberhart-Phillips, Seismicity and geometry of a 110-km-long blind thrust fault, 1, The 1985 Kettleman Hills, California, earthquake, *J. Geophys. Res.*, *97*, 4843–4864, 1992.
Gee, L. S., R. A. Uhrhammer, and B. Romanowicz, Source parameters and rupture characteristics of the Gorda basin earthquakes and their tectonic implications (abstract), *Eos Trans. AGU*, *72* (44), Fall Meet. Suppl., 312, 1991.
Gu, G., and W. H. Prescott, Discussion on displacement analysis: Detection of crustal deformation, *J. Geophys. Res.*, *91*, 7439–7446, 1986.
Hanks, T. C., and H. Kanamori, A moment magnitude scale, *J. Geophys. Res.*, *84*, 2348–2350, 1979.
Heaton, T. H., and S. H. Hartzell, Earthquake hazards on the Cascadia subduction zone, *Science*, *236*, 162–168, 1987.
Heaton, T. H., and H. Kanamori, Seismic potential associated with subduction in the northwestern United States, *Bull. Seismol. Soc. Am.*, *75*, 933–942, 1984.
Holland, J. H., Genetic algorithms, *Sci. Am.*, *267*, 66–72, 1992.
Hudnut, K. W., M. H. Murray, A. Donnellan, Y. Bock, P. Fang, Y. Feng, Z. Shen, B. Hager, T. Herring, and R. King, Co-seismic displacements of the 1994 Northridge, California, earthquake (abstract), *Eos Trans. AGU*, *75*(44), Fall Meet. Suppl., 176, 1994.
Jennings, C. W., Fault activity map of California and adjacent areas, with locations and ages of recent volcanic eruptions. Calif. Div. of Mines and Geol., Sacramento, 1994.
Kelsey, H. M., and G. A. Carver, Late Neogene and Quaternary tectonics associated with northward growth of the San Andreas fault, Northern California, *J. Geophys. Res.*, *93*, 4797–4819, 1988.
King, G. C. P., R. S. Stein, and J. B. Rundle, The growth of geological structures by repeated earthquakes, 1, Conceptual framework, *J. Geophys. Res.*, *93*, 13,307–13,318, 1988.
Kirkpatrick, S., J. C. D. Gelatt, and M. P. Vecchi, Optimization by simulated annealing, *Science*, *220*, 671–680, 1983.
Lajoie, K. R., A. M. Sarna-Wojcicki, and Y. Ota, Emergent Holocene marine terraces at Ventura and Cape Mendocino, California—Indicators of high tectonic uplift rates (abstract), *Geol. Soc. Am. Abstr. Programs*, *14*, 178, 1982.
Lisowski, M., J. C. Savage, and W. H. Prescott, The velocity field along the San Andreas fault in central and southern California, *J. Geophys. Res.*, *96*, 8369–8389, 1991.
Marshall, G. A., Unraveling the paradox of the Loma Prieta leveling data: Where's the fault (abstract), *EOS Trans. AGU*, *73*(43), Fall Meet. Suppl., 123, 1992.
Marshall, G. A., and R. S. Stein, Elevation changes associated with the October 17, 1989, Loma Prieta, California, earthquake and their use to infer fault slip geometry, in *The Loma Prieta, California, Earthquake of October 17, 1989—Main-Shock Characteristics*, edited by P. Spudich, *U.S. Geol. Surv. Prof. Pap., 1550-A*, in press, 1996.
Matsu'ura, M., and T. Sato, A dislocation model for earthquake cycle at convergent plate boundaries, *Geophys. J.*, *96*, 23–32, 1989.
McLaughlin, R. J., W. V. Sliter, N. O. Frederiksen, W. P. Harbert, and D. S. McCulloch, Plate motions recorded in tectonostratigraphic terranes of the Franciscan complex and evolution of the Mendocino triple junction, northwestern California, *U.S. Geol. Surv. Bull. 1997*, 60 pp., 1993.
McPherson, R. C., and L. A. Dengler, The Honeydew earthquake August 17, 1991, *Calif. Geol.*, *45*, 31–39, 1992.
Merritts, D., and W. B. Bull, Interpreting Quaternary uplift rates at the Mendocino triple junction, northern California, from uplifted marine terraces, *Geology*, *17*, 1020–1024, 1989.
Okada, Y., Surface deformation due to shear and tensile faults in a half-space, *Bull. Seismol. Soc. Am.*, *75*, 1135–1154, 1985.
Oppenheimer, D. H., and M. E. Magee, The 1991 M6.0 Honeydew, California earthquake (abstract), *Eos Trans. AGU*, *72* (44), Fall Meet. Suppl., 311–312, 1991.
Oppenheimer, D., et al., The Cape Mendocino, California, earthquake sequence of April, 1992: Subduction at the triple junction, *Science*, *261*, 433–438, 1993.
Prescott, W. H., The determination of displacement fields from geodetic data along a strike-slip fault, *J. Geophys. Res.*, *86*, 6067–6072, 1981.
Press, F., Earth models obtained by Monte-Carlo inversion, *J. Geophys. Res.*, *73*, 5223–5234, 1968.
Savage, J. C., A dislocation model of strain accumulation and release at a subduction zone, *J. Geophys. Res.*, *88*, 4984–4996, 1983.
Savage, J. C., and W. H. Prescott, Precision of Geodolite distance measurements for determining fault movements, *J. Geophys. Res.*, *78*, 6001–6008, 1973.
Savage, J. C., W. H. Prescott, and G. Gu, Strain accumulation in southern California, 1973–1984, *J. Geophys. Res.*, *91*, 7455–7473, 1986.
Smith, S. W., and J. S. Knapp, The northern termination of the San Andreas fault, in *Studies of the San Andreas fault zone in northern California*, edited by R. Strietz and R. Sherburne, *Spec. Rep. Calif. Div. Mines Geology*, *140*, 153–164, 1980.
Stein, R. S., Discrimination of tectonic displacement from slope-dependent errors in geodetic leveling from southern California, 1953–1979, in *Earthquake Prediction—An International Review*, *Maurice Ewing Ser.*, vol. 4, edited by D. W. Simpson and P. G. Richards, pp. 441–456, AGU, Washington, D.C., 1981.
Stein, R. S., and G. Ekström, Seismicity and geometry of a 110-km-long blind thrust fault, 2. Synthesis of the 1982–1985 California earthquake sequence, *J. Geophys. Res.*, *97*, 4865–4883, 1992.
Stein, R. S., G. C. P. King, and J. B. Rundle, The growth of geological structures by repeated earthquakes, 2, Field examples of continental dip-slip faults, *J. Geophys. Res.*, *93*, 13,319–13,331, 1988.
Stein, R. S., G. A. Marshall, and M. H. Murray, Permanent ground movement associated with the 1992 $M=7$ Cape Mendocino earthquake: Implications for damage to infrastructure and hazards to navigation, *U.S. Geol. Surv. Open File Rep. 93-383*, 40 pp., 1993.
Strand, R. G., Redding Sheet, Geologic Map of California, edited by Olaf P. Jenkins, Calif. Div. of Mines and Geol., Sacramento, 1962.
Toppozada, T. R., and D. L. Parke, Areas damaged by California earthquakes, 1900–1949, *Open File Rep. 82-17 SAC*, Calif. Div. of Mines and Geol., Sacramento, 1982.
Wang, Y., R. A. Prade, J. Griffith, W. E. Timberlake, and J. Arnold, A fast random cost algorithm for physical mapping, *Proc. Natl. Acad. Sci. U. S. A.*, *91*, 11,094–11,098, 1994.
Wilson, D. S., A kinematic model for the Gorda deformation zone as a diffuse southern boundary of the Juan de Fuca plate, *J. Geophys. Res.*, *91*, 10,259–10,270, 1986.
Wilson, D. S., Deformation of the so-called Gorda plate, *J. Geophys. Res.*, *94*, 3065–3075, 1989.
Wilson, D. S., Confidence intervals for motion and deformation of the Juan de Fuca plate, *J. Geophys. Res.*, *98*, 16,053–16,071, 1993.

M. Lisowski, Hawaii Volcano Observatory, P.O. Box 51, Hawaii National Park, HI 96718 (e-mail: mlisowski@tako.wr.usgs.gov).
G. A. Marshall, Trimble Navigation Ltd., Surveying and Mapping Systems, 485 Potrero Avenue, Sunnyvale, CA 94086 (e-mail: grant_marshall@trimble.com).
M. H. Murray, Department of Geophysics, Mitchell Building, Stanford University, Stanford, CA 94305-2215 (e-mail: mmurray@pangea.stanford.edu).
R. S. Stein, U.S. Geological Survey, 345 Middlefield Road, MS 977, Menlo Park, CA 94025 (e-mail: rstein@isdmnl.wr.usgs.gov).

(Received November 21, 1994; revised July 7, 1995;
accepted August 21, 1995.)